2011

Turbulent flow separation in three-dimensional asymmetric diffusers

Elbert Jeyapaul
Iowa State University

Turbulent flow separation in three-dimensional asymmetric diffusers

by

Elbert Jeyapaul

A dissertation submitted to the graduate faculty

in partial fulfillment of the requirements for the degree of

DOCTOR OF PHILOSOPHY

Major: Aerospace Engineering

Program of Study Committee:

Paul A. Durbin, Major Professor

Zhi J. Wang

Hui Hu

Alric P. Rothmayer

James C. Hill

Iowa State University

Ames, Iowa

2011

TABLE OF CONTENTS

LIST OF TABLES

LIST OF FIGURES

NOMENCLATURE

p	static pressure
x	streamwise distance
ρ	DensityVariable value vector
Q	Flow rate, m^3/s
A	Cross sectional area, m^2
α	tangent of top flare angle
β	tangent of side flare angle
C_μ	Coefficient of eddy–viscosity
C_p	Coefficient of pressure
$\boldsymbol{S}$	Non-dimensional strain tensor
AR	Aspect ratio
a_{ij},$\mathbf{a}$	Turbulence anisotropy tensor
$\overline{u_i u_j}$	Reynolds stress tensor
U,V,W	Mean flow velocity components
u,v,w	Fluctuating velocity components
Subscripts	
sgs	Subgrid Scale
r	Reference diffuser
0	diffuser inlet
+	Non-dimensional wall units
x,y,z	Cartesian coordinates
Greek symbols	
δ_{ij}	Kronecker delta
ε	Dissipation rate

κ	Von Karman constant
τ_{ij}	Stress tensor
$\mathcal{P}/\varepsilon$	Production-to-dissipation ratio
ν	Kinematic viscosity
$\alpha,\ \beta$	Tangents of top and side flare angles
β_i	Scalar coefficient of tensor polynomial basis 'i'
$\boldsymbol{\Omega}$	Non-dimensional vorticity tensor

Abbreviation

SST	Shear Stress Transport
DES	Detached Eddy Simulation
LES	Large Eddy Simulation
SAS	Scale Adaptive Simulation
RANS	Reynolds–Averaged Navier Stokes
EARSM	Explicit Algebraic Reynolds Stress Model

ACKNOWLEDGEMENTS

xiii

ABSTRACT

Turbulent three-dimensional flow separation is more complicated than 2-D. The physics of the flow is not well understood. Turbulent flow separation is nearly independent of the Reynolds number, and separation in 3-D occurs at singular points and along convergence lines emanating from these points. Most of the engineering turbulence research is driven by the need to gain knowledge of the flow field that can be used to improve modeling predictions. This work is motivated by the need for a detailed study of 3-D separation in asymmetric diffusers, to understand the separation phenomena using eddy-resolving simulation methods, assess the predictability of existing RANS turbulence models and propose modeling improvements. The Cherry diffuser has been used as a benchmark. All existing linear eddy-viscosity RANS models $k-\omega$ SST,$k-\epsilon$ and v^2-f fail in predicting such flows, predicting separation on the wrong side. The geometry has a doubly-sloped wall, with the other two walls orthogonal to each other and aligned with the diffuser inlet giving the diffuser an asymmetry. The top and side flare angles are different and this gives rise to different pressure gradient in each transverse direction. Eddy-resolving simulations using the Scale adaptive simulation (SAS) and Large Eddy Simulation (LES) method have been used to predict separation in benchmark diffuser and validated. A series of diffusers with the same configuration have been generated, each having the same streamwise pressure gradient and parametrized only by the inlet aspect ratio. The RANS models were put to test and the flow physics explored using SAS-generated flow field. The RANS model indicate a transition in separation surface from top sloped wall to the side sloped wall at an inlet aspect ratio much lower than observed in LES results. This over-sensitivity of RANS models to transverse pressure gradients is due to lack of anisotropy in the linear Reynolds stress formulation. The complexity of the flow separation is due to effects of lateral straining, streamline curvature, secondary flow of second kind, transverse pressure gradient on turbulence. Resolving these effects is possible with anisotropy turbulence models as the Explicit

Algebraic Reynolds stress model (EARSM). This model has provided accurate prediction of streamwise and transverse velocity, however the wall pressure is under predicted. An improved EARSM model is developed by correcting the coefficients, which predicts a more accurate wall pressure. There exists scope for improvement of this model, by including convective effects and dynamics of velocity gradient invariants.

CHAPTER 1.   OVERVIEW

Aerodynamic flows are mostly streamlined and characterized by large irrotational regions, in which motion is dictated by a balance between convection and pressure gradients and a relatively thin rotational layer. Turbulent mechanisms play an important role only in the highly sheared regions such as boundary layers, wakes and separated mixing layers. While the fundamental turbulence mechanisms are complex even in attached flows, the engineer is only interested in a few global manifestations of turbulence, that are dictated by a statistical turbulence variables. This focus allows highly simplified turbulence modeling approaches, such as the eddy viscosity. These models side-step the underlying physics and rely heavily on empirical correlations and constants derived from basic idealized flows. Flows in which turbulence plays a more influential role than in boundary layers require refined turbulence modeling. Among these are turbulent flow separation and recirculation caused due to adverse pressure gradients. Separations often occur at the limits of the design envelope and cause a loss in performance; hence it is of much interest to turbulence modeling research.

Separation can be induced by adverse pressure gradient or by geometric singularity; the former is discussed in this thesis. Turbulent separation is characterized by increased strain rates and higher production-to-dissipation ($\mathcal{P}/\varepsilon$) ratio. Two-dimensional separation is well understood and most eddy-viscosity models produce accurate prediction of wall shear stress and pressure in up to moderate strain rates. At high strain rates, the log region of the boundary layer deviates from equilibrium, i.e. $\mathcal{P}/\varepsilon \gg 1$, which makes the Reynolds stress-intensity ratio to be greater than $\sqrt{C_\mu}$, hence standard eddy-viscosity models fail. This shortcoming was fixed in k-ω SST model by Menter (1994) using a stress limiter in the eddy-viscosity calculation. Three-dimensional separation is more complicated than in 2-D.

Unlike two-dimensional flows, where separation occur at the zero wall shear stress, in 3-

D separation can occur at singular points and along convergence lines emanating from these points. Hence critical point theory using the wall-limiting streamlines (Tobak and Peake, 1982) is a common way to describe 3-D separation. Moreover, the flow separation is nearly independent of the Reynolds number. A number of experiments have been conducted to study 3-D flow separation, notably are asymmetric diffuser (Cherry et al., 2008) and flow over a hill (Byun and Simpson, 2006, NASA Fundamental Aerodynamic Investigation of The Hill experiment). These are smooth wall separations, induced by APG and Reynolds stress anisotropy, unlike separation separation due to obstruction — as in wing-body junction or cross-flow separation over a prolate spheroid or afterbody separation. In these flows, interacting 3-D turbulent boundary layers play an important role in creating secondary flow effects of second kind. As opposed to external flow, internal flow separation is more influenced by these secondary effects due to Reynolds stresses and only models that resolve secondary effects succeed in accurately predicting 3-D separation. Cherry's diffuser has proven a challenge to linear eddy-viscosity models, which predict separation on the wrong wall of the diffuser, hence topologically incorrect. Engineering turbulence research today is driven by the need to gain knowledge that can be used to improve modeling predictions. The thesis work is motivated by the need for a detailed study of 3-D separation in diffusers, to understand the separation phenomena and propose modifications to improve the predictability of Reynolds-Averaged Navier Stokes (RANS) turbulence models.

1.1 Separation definition

Separation is the entire process of departure, or breakaway, of the boundary layer from a wall; or the breakdown of the boundary layer assumption. The separation surface is the surface that bounds the zone between the separated shear layer and the wall. Researchers have studied turbulent separation over the years, but each with a different definition of the separation surface/line. Hence there is need for a unified definition of separation line/surface. A collection of these definitions presented in Törnblom (2006), are;

- recirculation region with dividing streamline connecting stagnation points on wall.

- curve/surface of zero Streamwise velocity

- region with backflow more than 50% of the time (Simpson, 1989)

Here the locus of zero Streamwise velocity is adopted, as the average flow field is steady. Turbulent flow separation is best identified at the wall, rather than within the flow field, as the flow becomes two dimensional. Simpson (1996) defines the kind of separation from the percentage of time the wall shear stress reverses sign. An intermittent transitory detachment is when τ_{wall} reverses sign 20% of time and detachment is when $\overline{\tau_{wall}} = 0$, which is the case in the diffusers studied. Only pressure-induced separation occurs in diffusers, due to the gradual expansion.

1.2   Background

Though three-dimensional separated flow is highly chaotic and no straight forward extension exists from 2-D separation concepts, there has been a number of efforts to develop a rational approach to analyze these flows. Experimentalist rely more on wall stress signature (oil streaks) to characterize separation, and the mean flow streamlines in the bulk flow to analyze the vortex structures (Délery, 2001). Legendre (1956) proposed analyzing the wall stresses using the geometric theory of two-dimensional smooth vector fields: one locates the zeros, singular/critical points of the skin friction field, identifies their stability type, then constructs the phase portrait of skin-friction trajectories. This critical point based approach has been adopted and extended by Tobak and Peake (1982), Chapman and Yates (1991) and Chong et al. (1990). In a general view, Lighthill (1963) proposed that convergence of skin friction lines is a necessary criterion for separation. He went on to deduce that separation lines always start from saddle-type skin-friction zeros and terminate at stable spirals or nodes. A review of terminologies and separation topologies are given in Délery (2001). Haimes and Kenwright (1999) have used critical point theory and extended it to analyze velocity gradient of the flow to extract features. Feature extraction studies have been quite helpful in knowing separation flow features and topologies and also the vortex cores though Eigen analysis of the vorticity tensor. Recently, an extended description of three-dimensional steady flow separation has been developed by Surana et al. (2006) using wall stress lines.

All the methods used above have been quite helpful in computational studies of 3-D separated flows. Time-resolving simulations have also provided information about higher-order statistics. Such studies are useful in understanding the mechanism of interaction between the mean flow and Reynolds stresses. Studies in 2-D planar diffusers primarily use the data set of Obi et al. (1993), which was repeated and extended by Buice and Eaton (2000). Obi et al. (1993) used a high aspect ratio inlet to eliminate the 3-D effect.

However as the inlet aspect ratio is reduced to about 4:1, a 3-D separation bubble begins to form. Experiments in 3-D asymmetric diffuser first performed by Cherry et al. (2008) indicate the separation behavior to be very sensitive to minor geometric changes. In their work, two doubly-sloped diffusers were tested at a Reynolds number of 10,000 based on inlet half height. Both diffusers have the same inlet cross-sectional area and aspect ratio, and the the same length and outlet areas that differed by less than 6%,; nevertheless, their separation bubbles developed very differently. The first diffuser has been used as a benchmark at a workshop [1], as RANS models fail miserably for this case. Most of the researchers studied the flow using eddy-resolving simulations; Breuer et al. (2009) studied the flow using a Hybrid LES-RANS(HLR) with EARSM formulation in RANS regions. A similar simulation approach was used by Abe and Ohtsuka (2010); Gross and Fasel (2010), Uribe et al. (2010) used the SAS model. LES using the dynamic Smagorinsky model performed by Terzi et al. (2010); Schneider et al. (2010) have predicted separation accurately. Both these simulation have used wall functions to predict the separation accurately. DNS results of Ohlsson et al. (2010) have provided high fidelity data set for this diffuser.

1.3 Asymmetric diffuser

Three-dimensional diffusers having an asymmetric sloped wall in both transverse directions are termed asymmetric. These diffusers have two adjacent walls that are sloped from the inlet channel, while the other two walls that are adjacent remain orthogonal though the length of diffuser. The configuration of the diffusers is as shown in Figure 1.1. Because two walls slope linearly, the cross-sectional area increases quadratically with streamwise distance. The aspect

---

[1]ERCOFTAC workshop on Refined Turbulence modeling, Rome(2008) and Graz(2009)

ratio of the cross section increases or decreases depending on the slope angles. The inlet to the diffuser is a straight, rectangular cross-section duct and is sufficiently long to generate a fully developed turbulent flow.
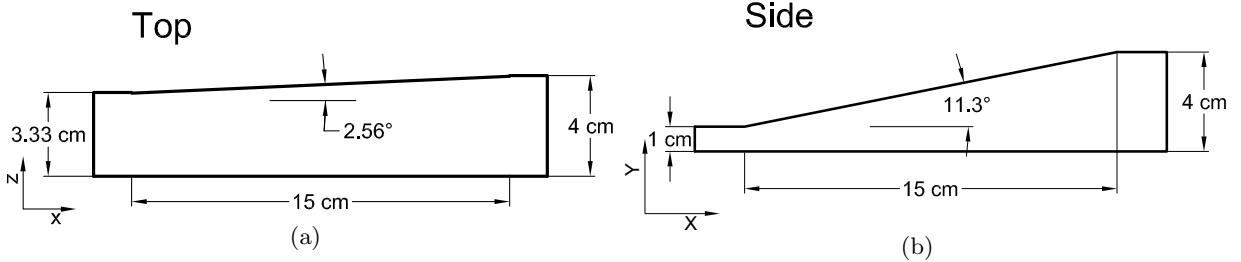
Figure 1.1   Dimensions of Cherry's diffuser 1 (Cherry et al., 2008)

Turbulent flow in rectangular channels is fundamentally complex. A delicate balance between the mean streamwise flow and gradients of Reynolds stress create secondary currents, called Prandtl's secondary flow of second kind. An analysis of the mechanism of fully-developed flow in square ducts is presented by Huser et al. (1994). The turbulence anisotropy generates secondary flow vorticity. Consider the streamwise mean vorticity equation

$$V\partial_y\Omega_x + W\partial_z\Omega_x = \nu(\partial_y^2\Omega_x + \partial_z^2\Omega_x) + \partial_y\partial_z(\overline{v^2} - \overline{w^2}) - \partial_y^2\overline{vw} + \partial_z^2\overline{vw} \tag{1.1}$$

where $\Omega_x = \partial_y W - \partial_z V$ and y,z are the coordinates in transverse directions. In turbulent flow, the last three terms become sources for mean streamwise vorticity. The first involves normal stress anisotropy ($\overline{v^2} \neq \overline{w^2}$) and the next two terms involve secondary stress ($\overline{vw}$), 'secondary' as they involve components in the secondary/transverse plane of flow. Near the wall, a two-component limit is reached as $\overline{v^2} \ll \overline{u^2}$. Due to anisotropy, two counter rotating vortices are formed towards each of the corners of the duct. Fully-developed flow is in turbulent equilibrium, and is supported by a constant mean streamwise pressure gradient that balances the wall shear stress. However when the flow enters the diffuser, additional effects as lateral straining, streamline curvature, transverse pressure gradients, non-linear streamwise pressure gradient drive the flow away from turbulence equilibrium. These effects influence turbulence anisotropy and eventually the reverse flow in the diffuser.

The presence of these effects in this diffuser configuration, has made it a suitable geometry

to study the physics of turbulent 3-D separation and to benchmark, developed turbulence modeling refinements.

1.4 Reynolds number dependence

The simulations for the Asymmetric diffuser were conducted at Reynolds numbers of 10,000 and 20,000 based on the inlet bulk velocity and channel half-height (y-direction). For a fully-developed square duct, it is know that the stress anisotropy remains the same as the Reynolds number is increased, however the near-wall velocity gradients increase. Délery (2001) reported that 3-D separation is nearly independent of the Reynolds number, which is, in fact, the correct scaling parameter in boundary-layer-like situations where viscous effects are confined within thin layers. This allowed them to study separation in high-Re supersonic flows in water tunnels. Experiments in a 3-D diffuser by Cherry et al. (2009) at Reynolds numbers of 10,000, 20,000 and 30,000 indicate the wall(y-minimum) pressure coefficient, C_p, to increase monotonically with increase in Re, though the shape of the C_p curve remains the same. The effects of Reynolds number in 3-D diffuser separation is outside the scope of this thesis.

1.5 Outline of the Thesis

The first chapter introduces the reader to the complexity of 3-D separation in diffuser flows and configuration of diffusers that are considered for the study. In Chapter 2, the generation of a series of diffusers is elaborated. The CFD codes used for RANS and eddy-resolving studies are explained, their numerics and turbulence models. The computational model of the diffuser explains the geometry and mesh used for steady and unsteady simulations. The quality of the Eddy-resolving simulations is also assessed. The methods used for generating a fully-developed flow also are presented. Chapter 3 presents observations from the Detached Eddy and Large Eddy Simulations. Firstly, the simulations are validated against experiments and DNS data sets for the diffuser of Cherry et al. (2008). Simulations of a series of diffusers are then presented: the physics of the flow separation is analyzed though wall streamlines, vortex dynamics, secondary flow and Reynolds stresses. In Chapter 4, the separation predicted in

Cherry's diffuser and series of diffusers using steady flow simulations of standard turbulence models, both RANS and second-moment closure models are presented. Their shortcomings are presented and modeling ideas discussed. The importance of anisotropy is explained and the ability of a particular Explicit Algebraic Reynolds Stress Model(EARSM) to resolve the mean flow of separation accurately is discussed. Variants and refinements of this model are used to predict diffuser flows. The model coefficients for the standard pressure-strain rate term have been calibrated. Using the diffuser series cases, the short comings observed in the EARSM are listed. Anisotropy-resolving capabilities of the EARSM have been further explored in basic non-separating flows. Modeling refinements proposed are presented in for future work.

CHAPTER 2.   DIFFUSER SERIES

Cherry et al. (2008) performed experiments on two diffusers, each having the walls sloped differently. Both of the diffusers were used for validation of the present simulations. Diffuser 1 has an area expansion ratio of 4.8 and Diffuser 2 a ratio of 4.56; similar, though their wall flare angles are different. The separation surface shows sensitivity to the wall angles, with Diffuser 1 separating on the top and Diffuser 2 separating on the side. A more accurate comparison of diffusers can be made if they have the same pressure gradient (dp/dx) at every streamwise (x) location. Thus the streamwise adverse pressure gradients will be the same and the effect of transverse pressure gradients can be studied. This is the motivation for creating data on a new series of diffusers.

2.1   Quasi 1-D analysis

A Quasi one-dimensional analysis using Bernoulli's equation gives the pressure gradient:

$$\frac{dp}{dx} = \frac{\rho Q^2}{A^3}\frac{dA}{dx} \tag{2.1}$$

where, Q is the bulk flow rate and A the cross-sectional area. A series of diffusers is to be defined with varying flare angles, but all having the same A(x) and same Reynolds number of 20,000, based on channel hydraulic diameter. They are parametrized by the inlet aspect ratio R. A member of the family has a flared top wall defined by the coordinate $y_0 + \alpha x$ and a flared side wall with the coordinate $z_0 + \beta x$, where subscript 0 refers to diffuser inlet and α & β are tangets of top and side flare angles.

The Cherry et al. (2008) diffuser has a high pressure gradient at the inlet to diffuser as seen in Figure 2.1(b); this momentum source strains the flow immediately on entering the diffuser inducing separation. To reduce the incidence of inlet separation and to build a standardized

geometry, a set of diffusers are generated having the same pressure gradient as that of Obi's 2-D diffuser Obi et al. (1993). This 2-D diffuser has a milder pressure gradient.

A 3-D reference asymmetric diffuser is constructed to produce the same pressure gradient of Obi et al. (1993). Other parameters of the reference geometry are an inlet $Æ_r = 1$ and Reynolds number of $20,000$ based on hydraulic diameter. The family of diffusers only differ by inlet $Æ$, as shown below. The cross-sectional area of the reference duct (r) and any duct in the family are given by

$$A = (y_0 + \alpha x)(z_0 + \beta x) = (y_r + \alpha_r x)(z_r + \beta_r x) \tag{2.2}$$

Equating coefficients of x defines the family

$$y_0 z_0 = y_r z_r$$

$$y_0 \beta + \alpha z_0 = y_r \beta_r + \alpha_r z_r$$

$$\alpha \beta = \alpha_r \beta_r$$

which has the solution,

$$y_0 = y_r \sqrt{\frac{Æ_r}{Æ}}, \; z_0 = z_r \sqrt{\frac{Æ}{Æ_r}},$$
$$\alpha = \alpha_r \sqrt{\frac{Æ_r}{Æ}}, \; \beta = \beta_r \sqrt{\frac{Æ}{Æ_r}} \tag{2.3}$$

Thus the family is parametrized by the entrance $Æ \equiv z_0/y_0$ and the reference duct has $Æ_r = z_r/y_r = 1$. The molecular viscosity of the fluid had to be modified for each of the cases to maintain inlet $Re = 20,000$. The ratio of the expansion angles is:

$$\frac{\beta}{\alpha} = \frac{Æ}{Æ_r} \frac{\alpha_r}{\beta_r} \tag{2.4}$$

Increasing $Æ$ increases the lateral straining.

It has been verified that RANS predictions are qualitatively correct at lower aspect ratios. So the series will provide a systematic look at how discrepancies develop. The properties of the diffusers which are simulated is given in Table 2.1.

Aspect Ratio, $\mathcal{R}$	1	1.5	2	2.5	3
Side angle θ_s,deg	2.56	3.13	3.6	4.04	4.43
Top angle θ_t,deg	11.3	9.27	8.04	7.2	6.58
Inlet c/s, w×h cm	1.34×1.34	1.64×1.09	1.89×0.95	2.12×0.85	2.32×0.77
Hydraulic dia. ϕ	1.34	1.31	1.26	1.21	1.16
Exit c/s, w×h cm	2.01×4.38	2.46×3.56	2.84×3.08	3.18×2.75	3.48×2.51
Kin. Visc. ν, m^2/s	1.34e-5	1.31e-5	1.26e-5	1.21e-5	1.16e-5

Table 2.1   Family of diffusers generating same adverse pressure gradient

(a)

(b)
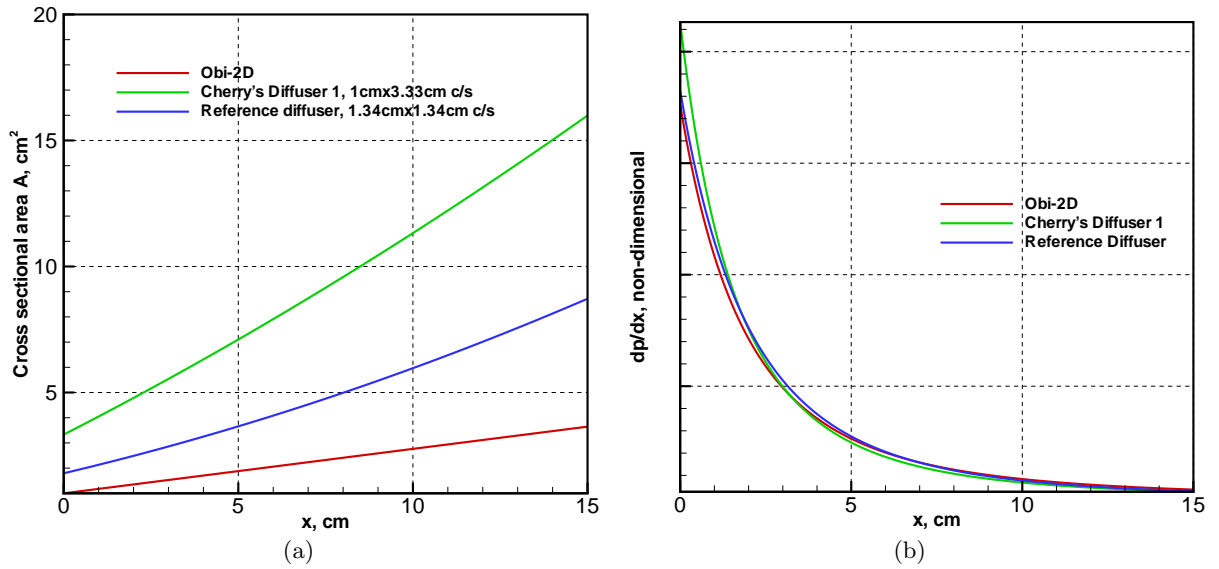
Figure 2.1   Area distribution(a) and streamwise pressure gradient(b) used in generating the diffuser series
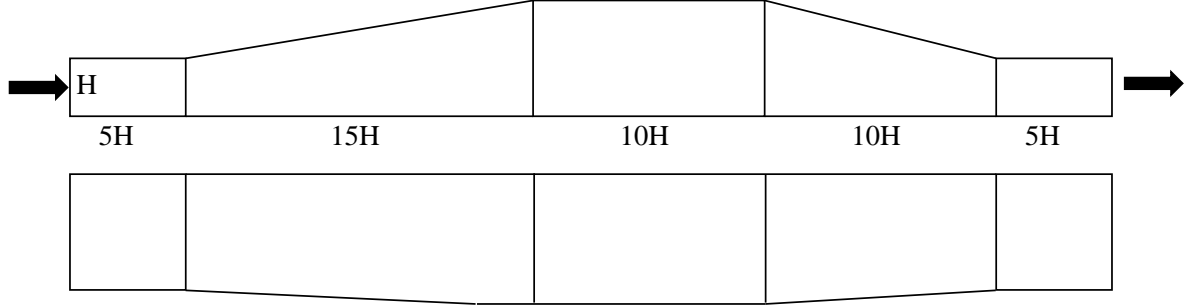
Figure 2.2   Outline of the diffuser domain used for simulations. Shown in side and top view.

2.2   Computational model

The computational flow domain includes an inlet channel to the diffuser and an outlet transition section after the diffuser. A typical flow domain is shown in Figure 2.2. The outlet transition section consists of a nozzle and rectangular channel to recover the pressure and ensure that no reverse flow exists at the domain outlet. A unidirectional flow would be suitable for a pressure outlet boundary condition in the CFD solver used. A constant area outlet section of $30H$ length was also considered , however the diffuser flow field was not different from that using a transition section. The experimental geometry has a filleted edge where the inlet channel joins the diffuser flared walls. This portion has been neglected in the computational model. A Diffuser 1 geometry with the filleting was constructed and simulated using LES, indicating no difference in the flow field except very close to the inlet.

The computational domain is discretized with hexahedral cells. The grid distribution for the RANS simulations uses a two surface mesh distribution with a Hermite interpolation method to ensure orthogonal grids near the wall. The number of grid points is $296 \times 41 \times 61$ along the x, y and z coordinates, a grid stretching of 1.2 was ensured near wall and a $y_+ \approx 0.5$. The grid is also clustered along the streamwise direction towards the diffuser inlet as shown in 2.3(a). The grid resolution for the DES was determined by performing a study. Two grids are used as below,

COARSE $357 \times 41 \times 61$, Near-wall expansion=1.1, $\Delta y_+ = 7$, $\Delta x_+ = 1640$ and $\Delta z_+ = 160$

FINE $296 \times 61 \times 101$, Near-wall expansion=1.01, $\Delta y_+ = 0.6$, $\Delta x_+ = 12$ and $\Delta z_+ = 36$

The wall units for the diffuser were measured at the region of maximum shear stress in the inlet channel. The flow predicted by the coarse mesh shows a separation over the top wall of the diffuser, while experiments indicate a separation skewed towards the doubly-sloped edge. The fine mesh predicts such a separation surface and hence was chosen for other simulations. The grid distribution is quite uniform as seen in Figure 2.3(b) to maintain a cell aspect ratio close to unity.

The LES also are sensitive to grid resolution as noticed by Schneider et al. (2010). A grid of 3 Million cells is used ($477 \times 61 \times 101$) and quality checks are performed to assess the fidelity of simulations. LES quality metric tests are described in the next section. The grid is about 4^3 times smaller than the DNS grid used by Ohlsson et al. (2010). The near-wall mesh had a maximum of $\Delta y_+ = 2$, $\Delta x_+ = 90$ and $\Delta z_+ = 10$. A large number of cells were required along the streamwise direction, to generate a fully-developed flow at the diffuser inlet channel.

(a) RANS grid   (b) DES grid
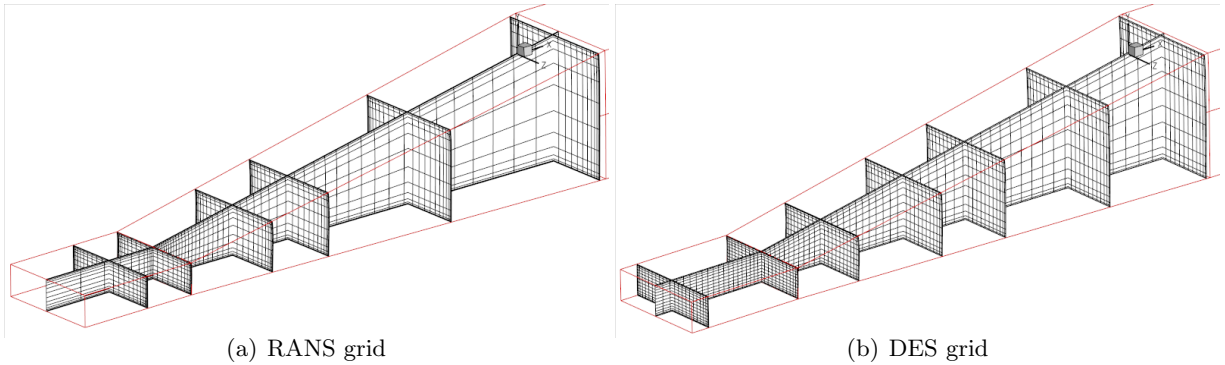
Figure 2.3   Mesh distribution in the diffuser showing every 4th node.

2.2.1   Codes and Numerics

Two codes were used for the RANS and eddy-resolving simulations. SuMB is used to perform the DES, while OpenFOAM is used for LES and RANS simulations. The turbulence model was implemented and validated in OpenFOAM.

2.2.1.1 SuMB

SuMB is a parallelized structured multi-block finite volume code (Van der Weide et al., 2006). Only a fully compressible solver is available, hence a preconditioner is required to apply it to low-Mach number flow. A few of the key parameter used for the solver are

- central with matrix dissipation for flux computations

- Roe's Riemann solver with Van Albeda limiter

- 5-stage Runge Kutta smoother for flow variables and ADI smoother for turbulence quantities

- 3W multigrid

- Turbulence production term only considers strain

- Maximum ratio of TKE-production/dissipation: 1e5

- Fractional Time-stepping method allows for CFL > 1

2.2.1.2 OpenFOAM

OpenFOAM is a parallelized unstructured finite volume code (www.openfoam.com). The incompressible solver is used with the following salient parameters:

- Conjugate gradient linear solver for pressure

- Bi-conjugate gradient solver for momentum

- The PISO algorithm is used with two corrector steps.

- To improve convergence, a limited central differencing is used for convective terms

- central difference for gradient and Laplacian terms

- second-order backward scheme is used for time derivatives.

- For RANS simulations, the SIMPLE method is used with Gauss-Seidel smoother for transport terms.

2.2.2 Inflow profile generation

For the SuMB simulations, a precursor simulation of flow in a plane channel was performed to generate the full-developed turbulent flow profile, to be used as an inlet to the diffuser flow. A channel with periodic inlet-outlet boundary condition was used. For DES the turbulence quantities are computed as,

$$k_{sgs} = \sqrt{\frac{2}{C_\mu}\nu_{sgs}|S|} \quad ; \quad \omega_{sgs} = \frac{\epsilon}{k} = \sqrt{2C_\mu}|S| \tag{2.5}$$

from an LES of periodic channel. Using this a database of the fields U, V, W, k_{sgs} and ω_{sgs} is stored in a 2-D plane, at equal intervals of time. This turbulence field is interpolated onto the inlet of DES based on the time step of the simulation. This method does not need a perturbed initial condition for the diffuser, as the inlet turbulence introduces that as flow iterations progress.

The LES did not require a precursor simulation, as *OpenFOAM* contains a feature to generate inflow for eddy resolving simulation. Data are mapped from a downstream plane upstream of the diffusing section to the inlet. Thereby, the initial section develops a fully-developed, turbulent profile. The mass flow through the mapping is fixed to the specified bulk flow. A random perturbation of the flow field is required to induce turbulence. Baba-Ahmadi and Tabor (2009) explain the flow mapping method. The length of the mapped domain is 10H as shown in Figure 2.4.

Mapped Inlet
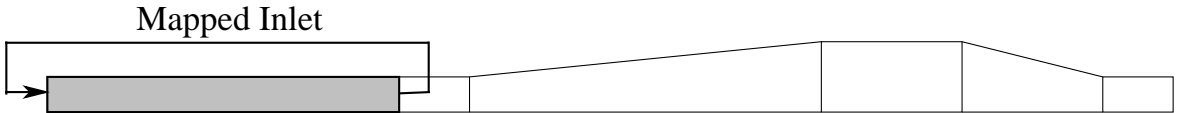
Figure 2.4   Flow domain with inlet mapping

The fully-developed flow predicted by the LES is shown in Figure 2.5. It also shows the secondary flow caused by turbulence anisotropy. Though this secondary flow magnitude is about 5% of U_{bulk}, it affects the separation structure.
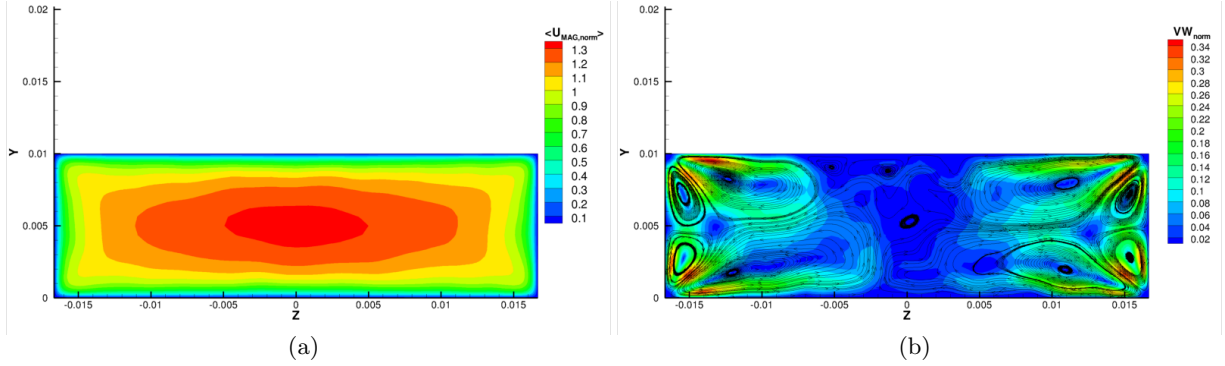
Figure 2.5   Primary and Secondary velocity profile in the fully-developed rectangular channel of $\mathcal{R}$=3.33. Statistics were averaged over 50 flow-through times.

2.2.3   Computing resources

All the simulations were performed in parallel on Linux SMP clusters. The MPICH standard is used for data transfer across compute nodes by both codes. SUMB required the number of grid nodes along each coordinate direction to be a multiple of 4 for 3-level Multigrid to be used. The DES was converged at every time level with 80 pseudo-time iterations, a large time step (10 times larger than LES) was possible, as the numerical time integration method was not limited by CFL criteria. The LES is most expensive as seen in Table 2.2, due to stringent near-wall grid requirement. Moreover, statistical averaging was required over a large flow-through times $\left(\frac{TU_\infty}{L}\right)$ to converge the high-frequency fluctuations, increasing the simulation time. Table 2.2 summarizes the typical compute resources for each simulation. The RANS compute times for both solvers were quite comparable. The EARSM simulations were initialized using SST-predicted flow field and simulated for 400 CPU hours to convergence level.

Simulation	Grid size ($\times 10^6$ cells)	CPU's	Wall time	CPU Hours
LES	3	128	27 days	83,944
DES	1.8	128	3.5 days	10,752
RANS – SUMB	1.2	64	17 hours	1,088
RANS – OpenFOAM	1	32	23 hours	736

Table 2.2   Computational resource for each Eddy-resolving and RANS simulation

CHAPTER 3. EDDY-RESOLVING SIMULATIONS

Separation being a highly unsteady phenomena, time-resolved simulations of the flow field were required to resolve the turbulent structures and the energy cascade. The LES and DES simulation methods described in this chapter are collectively referred to as 'eddy-resolving'. This nomenclature is primarily to distinguish them from the RANS computations.

3.1 Detached Eddy Simulations

While LES is capable of resolving eddies and the turbulence spectrum, it requires a large number of grid points in the near wall region. Most of the near wall structures need to be resolved in order to compute the turbulent boundary layers. DES is a hybrid LES/RANS model, introduced to alleviate the near-wall grid requirement. The boundary layer region is solved with RANS and the separated region with eddy simulation. The basic DES model switches from RANS to eddy simulation automatically, based on the distance to wall and local grid spacing. However there is an issue: if the near wall mesh is too fine, the RANS model can switch off. This was address by the Scale Adaptive Simulation (SAS) method of Menter et al. (2003). Here the length scale is dependent on the local flow variables, rather than on grid spacing. This allows the eddy resolved region to change dynamically, while preserving RANS near the wall. The length scale parameter used is

$$L_{\nu k} = \kappa \left| \frac{\partial U / \partial y}{\partial^2 U / \partial y^2} \right|$$

The k-ω Shear Stress Transport (SST) model of Menter (1994) is used in the RANS region. With the stress limiter, this RANS model has proved to predict 2-D separation accurately in a variety of APG boundary layer flows. A fine near wall mesh ($y_+ \approx 0.6$) allows the RANS model to be integrated to the wall, and no wall function is used.

Due to the low Reynolds number of the channel flow, well resolved simulations could be made with small sub-grid viscosity. The spectral resolution of the simulation is assessed by probing the time-varying streamwise velocity in the bulk flow and analyzing the power spectral density. From Figure 3.1 we notice 3 orders of frequency resolved, with the inertial range following the -5/3 slope. The energetic spectral range widens and increases in magnitude as the flow moves downstream. No periodic frequency is seen. Hence, the flow is statistically stationary and Reynolds averaging is synonymous with time averaging.

(a) Probe 1, x/H=3

(b) Probe 2, x/H=6

(c) Probe 3, x/H=9

(d) Probe 4, x/H=12
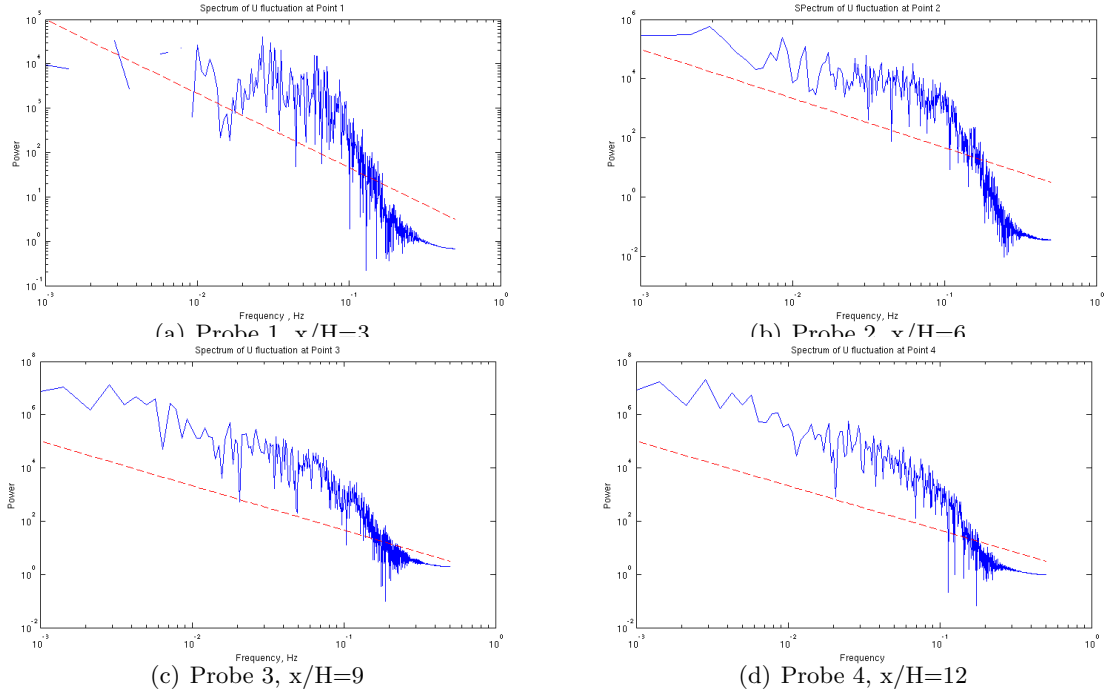
Figure 3.1   Power spectrum of instantaneous streamwise velocity. The 4 probe points are located at the centroid of cross-sectional planes that are equally spaced from inlet to outlet. The -5/3 slope line is in red.

The resolution of the turbulent energy is shown in Figure 3.2. The ratio of the resolved-to-total turbulent kinetic energy indicates that more than 50% of the energy is resolved. The eddy viscosity ratio is lower than 50 in the bulk of domain, except at the core of flow downstream where the mesh size is largest. These checks ensure the quality of DES results.

(a) $\frac{k_{RES}}{k_{RES}+k_{SGS}}$ (b) $\frac{\mu_T}{\mu}$
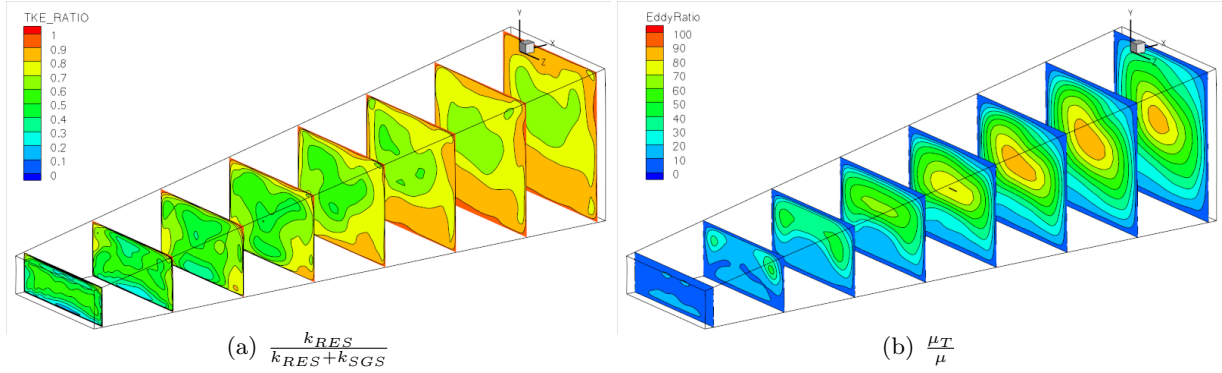
Figure 3.2 The ratio of the resolved-to-modeled turbulent energy in the baseline diffuser DES.

3.1.1 Validation

The Cherry et al. (2008) Diffuser 1 has been simulated and compared to experiments. This case will hereafter be referred as the baseline diffuser. The mean flow is calculated by averaging the flow over 10 flow-through (τ) times, with the averaging starting after 8τ. The streamwise velocities at transverse planes show a decent agreement with experiments (Figure 3.3). DES results shows a separation in the top left corner, which is absent in experimental data. The simulations predict the correct topology of separation on the top wall of the baseline case, though the volume of reverse flow is over-predicted. Too large reverse flow has also been predicted by hybrid LES-RANS simulations of Abe and Ohtsuka (2010) and SAS of Uribe et al. (2010). A detailed plot of the velocity at streamwise and spanwise locations is shown in Figure 3.4. The DES predictions indicate a higher velocity gradient close to the wall, which causes the pressure at the wall to be low, thus the pressure recovery in the diffuser is less than the experiment.

In contrast, the SST model predictions are qualitatively incorrect, separating on the wrong wall of the diffuser (Fig. 3.4). The secondary flow predictions did not agree with experiments either, but, as the secondary flow magnitudes are quite low ($\approx \%10 U_{bulk}$), their measurement accuracy are questionable.
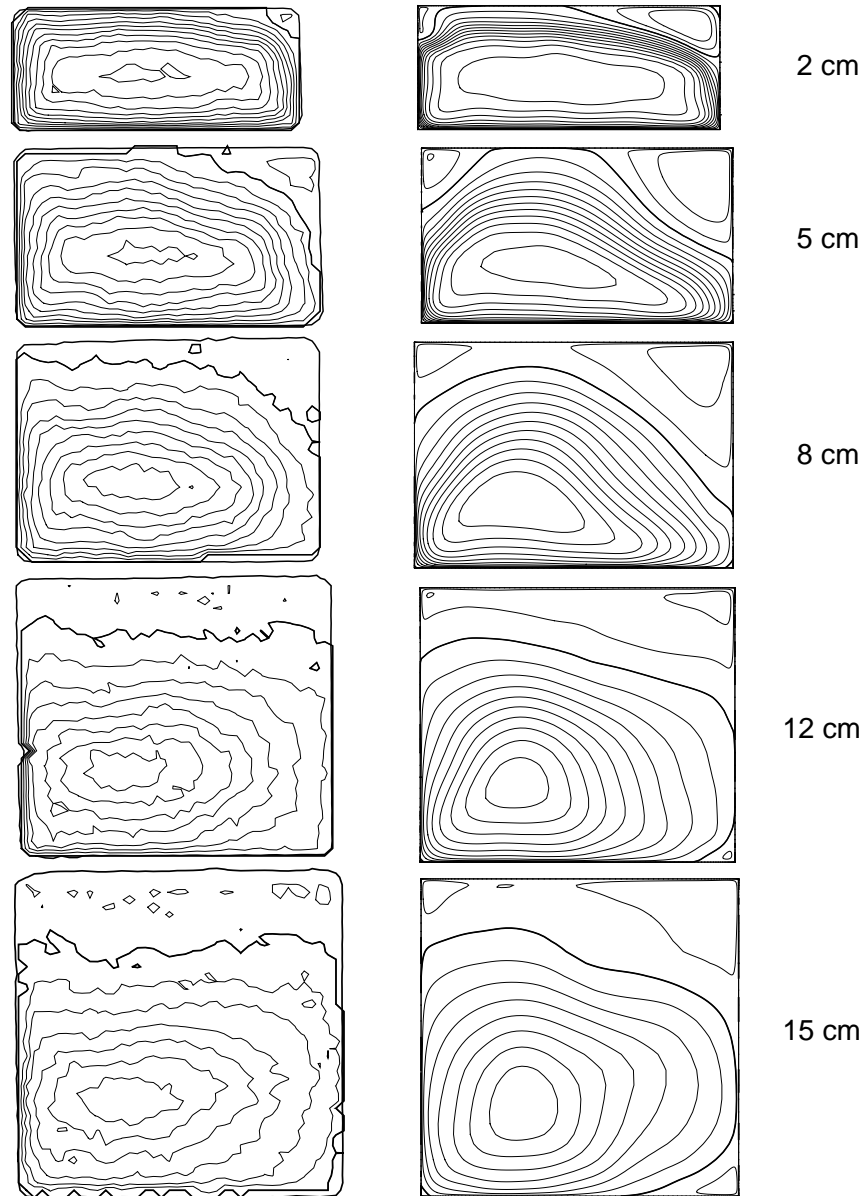
Figure 3.3 Streamwise velocity predicted using SAS and experimental measurements of Cherry et al. (2006) at transverse planes. Contour lines are spaced 0.1 m/s apart. The zero-streamwise-velocity contour line is thicker than the others.
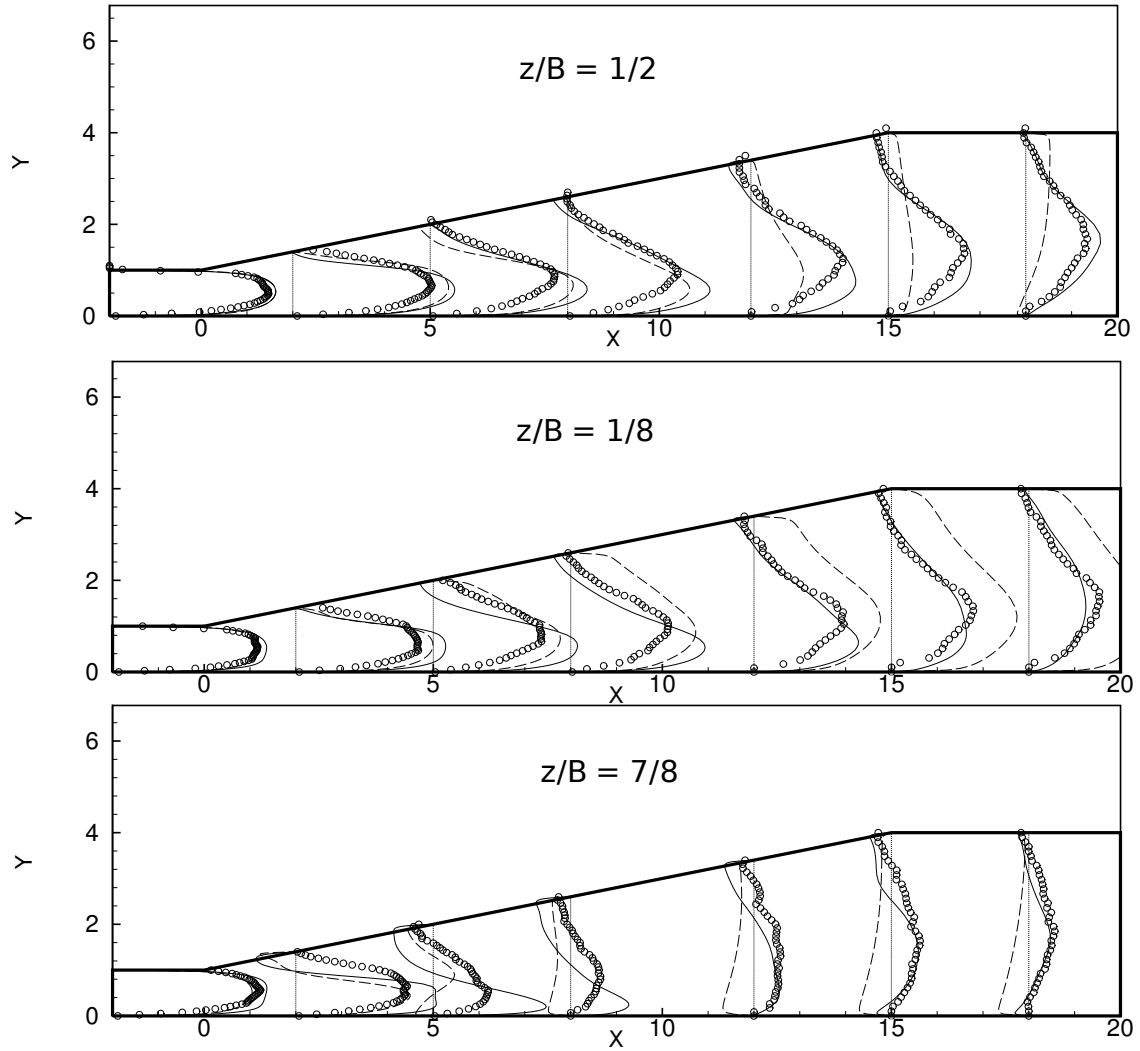
Figure 3.4   Variation of mean streamwise velocity along spanwise z-lines. B is the width of the diffuser at that x-location. The solid lines are DES, and dashed $k - \omega$ SST model compared with experimental data.

3.1.2   Study of flow separation

The computed DES results predict the correct separation topology and decent quantitative match with experiments. The wall-limiting streamlines on the baseline diffuser indicate where the flow separates from the wall. A number of nodal points are seen in Figure 3.5 on the sloped walls. Vortices originate from these singular points and convect through the boundary layer and reverse flow region. A clockwise vortex originates from a focus on the top wall and convects towards the side wall.
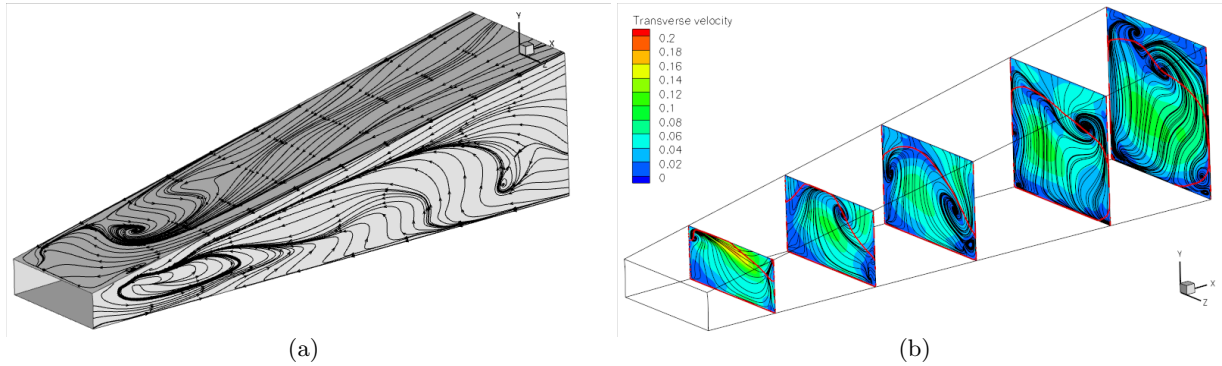
Figure 3.5   Secondary flow in baseline diffuser predicted by DES. (a) The wall limiting stream-
lines indicate the separation structure. (b) secondary flow at transverse planes
having streamwise vortices, the separation line is in red.

All of the two-equation RANS models predicted a transition of separation from top to side walls at about $\mathcal{R}2.5$. A DES of the series of diffusers is analyzed to know the efficacy of RANS models. These simulations indicated the averaged flow separation to be on the side wall for both $\mathcal{R}2$ and $\mathcal{R}2.5$. The results of $\mathcal{R}2.5$ are interesting as the flow is highly unsteady. In order that flow averaging be a meaningful way of analyzing the flow field, the unsteadiness has to be quantified. The flow intermittency is measured as the ratio of times the flow reverses to that of the streamwise direction. In Figure 3.6, the flow is unidirectionally streamwise towards the core of the diffuser, however values of 1 are observed towards the sloped corner and sides, indicating reverse flow to always exist there. Hence though the separation surface indicates partial separation on top, the separation is considered to be on the side wall. Movies of time-evolution of the separation surface show the separation surface to be attached to the side wall

consistently until half of the diffuser length, after which the separation moves between the top and side asymmetric walls. Analysis of the secondary flow in the diffuser series show an increase in secondary flow magnitude at $\mathcal{R}2.5$ as seen in Figure 3.7. Downstream of this diffuser, there exists a counter-clockwise churning, which convects flow from side to the top wall causing the separation surface ($\overline{U} \equiv 0$) to be unsteady.

(a) (b)
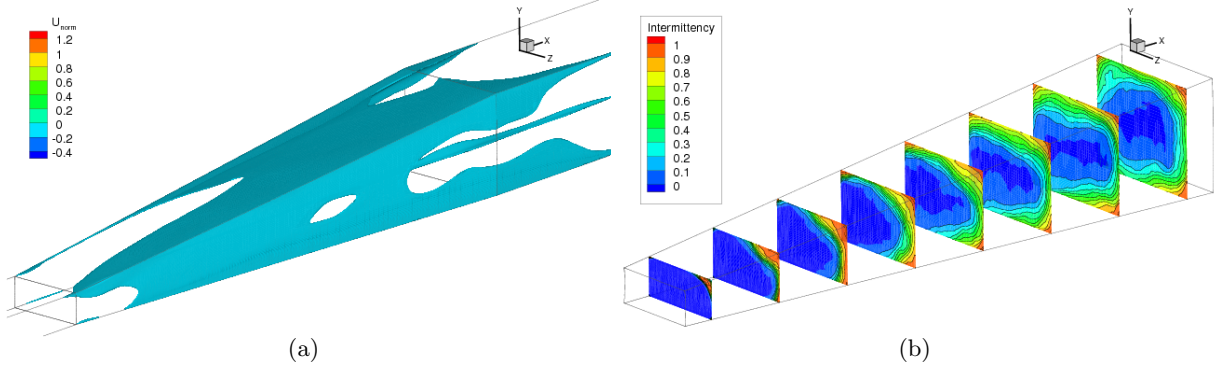
Figure 3.6 Separation bubble(a) and Intermittency(b) in the $\mathcal{R}2.5$ diffuser predicted using the DES model.

(a) $\mathcal{R}2$ (b) $\mathcal{R}2.5$
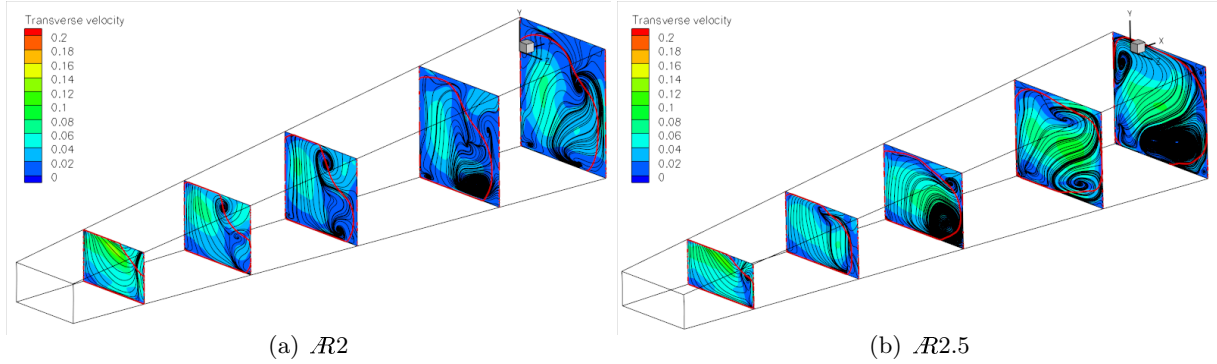
Figure 3.7 Secondary flow show a similarity in pattern at different inlet aspect ratios. The foci is formed earlier in the $\mathcal{R}2.5$ diffuser and moves downstream

3.1.3 Vortical flow features

While the secondary flow magnitudes are only about 5% of the bulk velocity, they provide critical insight into the dynamics of the flow. The flow contains streamwise vortices that interact downstream the diffuser. Resolving these vortices are a challenge to existing RANS models,

as they dissipate faster and also overpredict turbulence production at the vortex core. The limiting streamlines in Figure 3.8 identify the various singular points on the diffuser surface as foci and saddle nodes. The identification and classification of these nodes is made by a visual comparison of the nature of the streamlines at these critical points (Délery, 2001). The theory behind classifying these points is described in the previous reference, which could be used in automated classification of these points. The foci are identified by coiled streamlines that converge at the core where $\tau_l(l, m) = \tau_m(l, m) = 0$, where l and m are wall coordinates. The saddle nodes appear where streamlines converge or diverge by bending 90 deg. In $\mathcal{R}2.5$ there are 3 foci and one saddle node, the separation surfaces emanate from where the wall streamlines converge and flow attachment at locations where streamlines diverge. The wall shear stress is non-zero at separation/attachment surfaces, as there exists cross-flow along these surfaces. From each of the focus vortices originate as shown in Figure 3.8 and interact downstream.
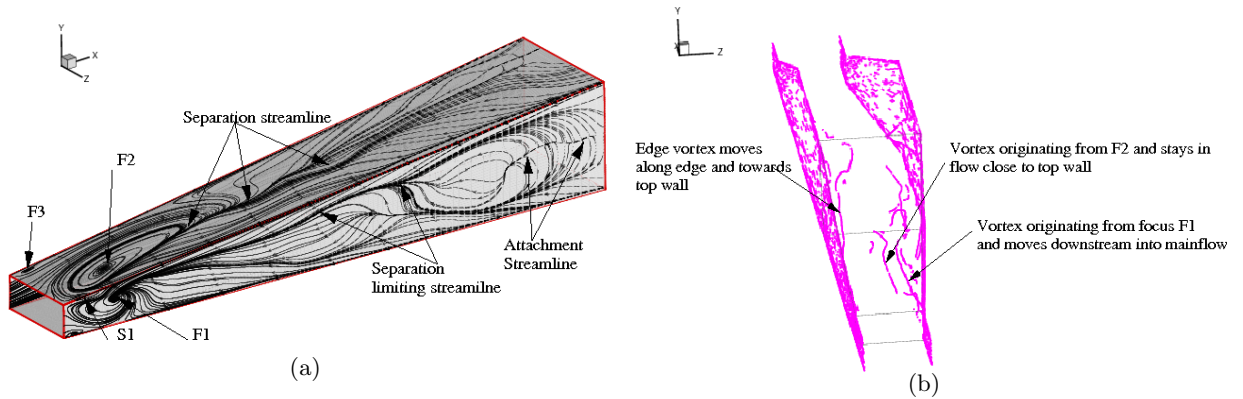
Figure 3.8   (a)Limiting streamlines for $\mathcal{R}2.5$ diffuser on the wall show a steady separation surface from the top wall, The side wall has a complex separation-attachment flow. (b)The vortex cores show a vortex originating from foci F3 on left and multiple vortices close to the double-sloped edge

The limiting steamlines on the diffuser cases $\mathcal{R}2$ and $\mathcal{R}2.5$ are identical, but the corresponding secondary flow inside the diffuser develops quite differently. Hence vortex interactions critically differentiate the flow in the series. For $\mathcal{R}2.5$, the wall streamlines have the singular points closer to the diffuser inlet than in $\mathcal{R}2$ (Jeyapaul and Durbin, 2010), hence there is more room for the vortices originating from them to develop along the APG boundary layer

and interact; which is the reason for high unsteadiness. As the flow enters the diffuser, the flow encounters transverse pressure gradients in addition to a much higher streamwise pressure gradient, which leads to secondary flow. Figure 3.9 shows flow moving diagonally away from the corner subjected to the APG. As the flow develops downstream, two vortices (at x/H=4) are introduced from the foci F1 and F2. These vortices interact and unify creating one vortex at x/H=5.8, this disintegrated downstream creating multiple vortex foci and a saddle node.

(a) x/H=1

(b) x/H=4

(c) x/H=5.8

(d) x/H=13.7
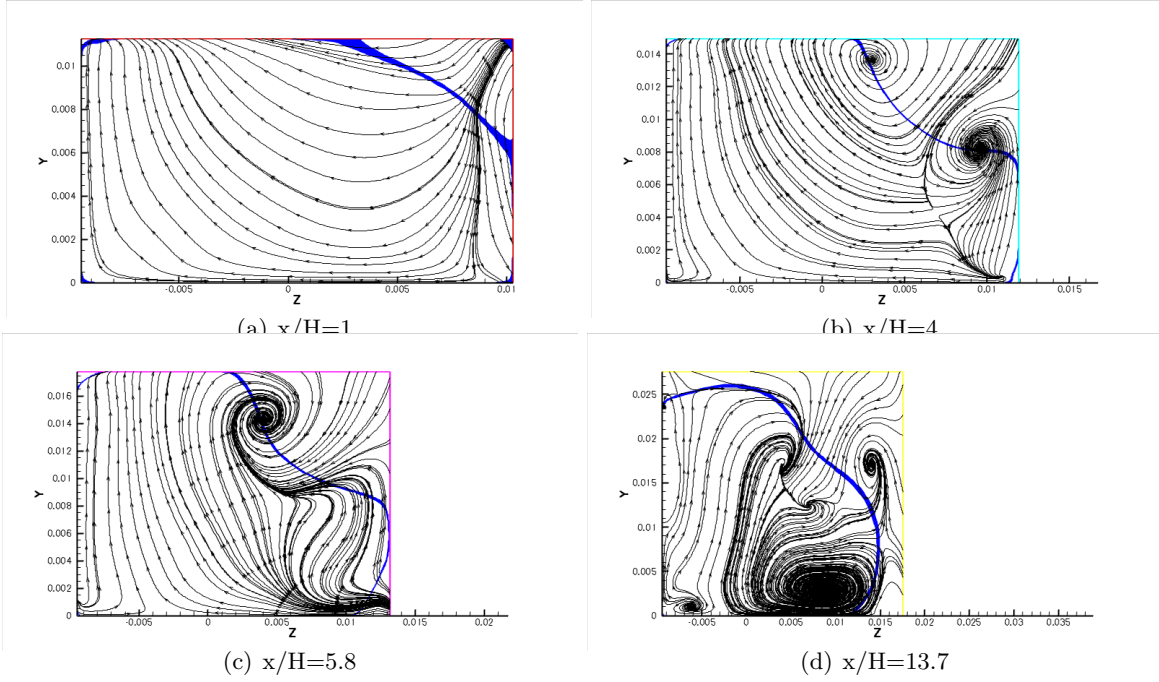
Figure 3.9   Secondary flow streamlines in transverse planes of $\mathcal{R}2$ diffuser. The blue line indicates the location of separation surface.

3.2   Large Eddy Simulations

LES are widely used to predict complex shear flows. The simulations were performed using the dynamic Smagorinsky model, in the incompressible solver of *OpenFOAM*. A test filter is performed on a larger size than the grid filter. The resolved Reynolds stresses in this 'test window' is representative of the sub-grid stresses and is used to evaluate C_s locally. Due to this, the model does not need near-wall damping. The effective SGS viscosity$(\nu + \nu_t)$ is set to zero in regions where the value becomes negative. The sub-grid stress is modeled by expression 3.1,

where sub-grid viscosity is given by $\nu_t = (C_s\Delta^2)|\overline{S}|$, which is a linear eddy-viscosity assumption.

$$\tau_{ij} - \frac{1}{3}\tau_{kk}\delta_{ij} = -2(C_s\Delta)^2|\overline{S}|\overline{S}_{ij}; \text{ where } |\overline{S}| \equiv \sqrt{2S_{ij}S_{ij}} \tag{3.1}$$

Since filtered Navier-Stokes equations change for different grid resolutions, the way to check the accuracy of the simulation is to compare the resolved first and second moments of the primitive flow variables. Celik et al. (2009) has a list of assessment measures to ensure the quality of LES. Errors in LES have the following sources: modeling, numerical and filtering. In order to isolate the modeling and discretization errors, a minimum of two to three grid calculations are necessary (Celik et al., 2009). In the interest of computational time, only a single grid case was used to check for LES errors. From the grid refinement studies with DES, the LES grid was arrived at with a refined near-wall grid with a cell expansion ratio of 1.05. The grid used for the simulation has 3 Million cells.

Single grid estimator checks were performed on this grid for the baseline diffuser. The spectrum of turbulence resolved by LES is indicated by a Fast Fourier analysis of data at point probes located along the bulk of the flow. The data were collected over 75 flow though times; the time required to converge mean flow statistics is shown in Figure 3.10. The frequency resolved spectrum is five orders of magnitude wide, as compared to 3 orders by the DES. We notice the inertial range to contain eddies whose energies cover by 3 orders of magnitude. The slope of this range does not follow Kolmogorov's scaling of -5/3. The reason for this higher slope is due to the low Reynolds number of the diffuser and also the non-homogeneity of the flow. The grid size used has a filter cut-off frequency of about 3×10^4Hz, which is the location where the spectrum changes slope. As this low energy region is relatively short, the error introduced due to sub-grid models is small.

The accuracy of the simulations was verified by a quantitative check on the amount of turbulent energy resolved:

$$\frac{k_{res}}{k_{tot}} = \frac{k_{res}}{k_{res} + k_{sgs} + |k_{num}|}$$

To evaluate the numerical error in the simulation, an LES on a different grid size would be required; in our check, the numerical error was neglected. About 95% of the turbulent kinetic

(a) Probe 1, x/H=3

(b) Probe 2, x/H=6

(c) Probe 3, x/H=9

(d) Probe 4, x/H=12
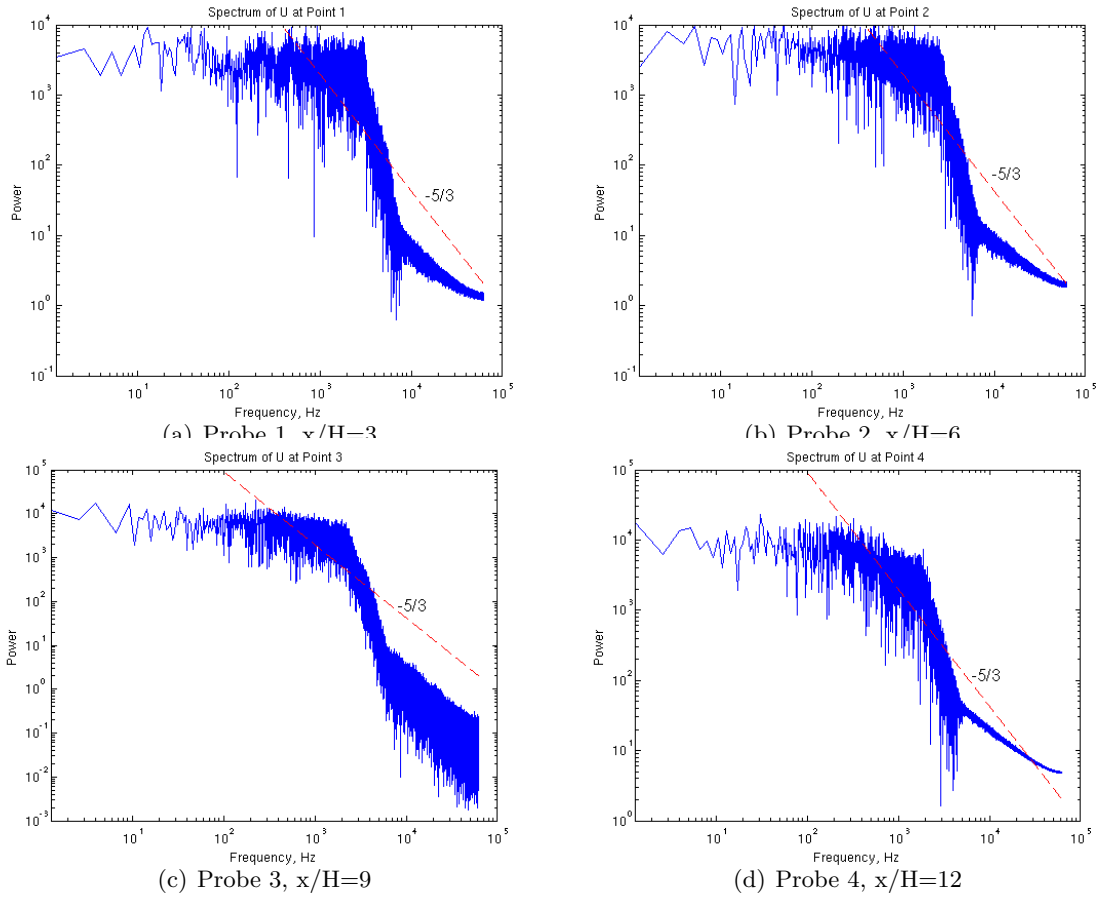
Figure 3.10 Power spectrum of instantaneous streamwise velocity predicted by LES. The 4 probe points are located at the centroid of cross-sectional planes that are equally spaced from inlet to outlet. The -5/3 slope line is in red.

energy is resolved (Figure 3.11), hence the flow is close to DNS resolution. Celik et al. (2009) suggested the calculation of a *relative sgs-viscosity index* as;

$$LES\_IQ_\nu = \frac{1}{1 + \alpha_\nu \left(\frac{\bar{\nu}_{eff}}{\nu}\right)^n}$$

where, $\nu_{eff} = \nu_{sgs} + \nu_{num} + \nu$ and $\alpha_\nu = 0.05$, n=0.53. This quantity is the ratio of eddy-viscosity and is close to 1 in the flow, which, hence, is well resolved.
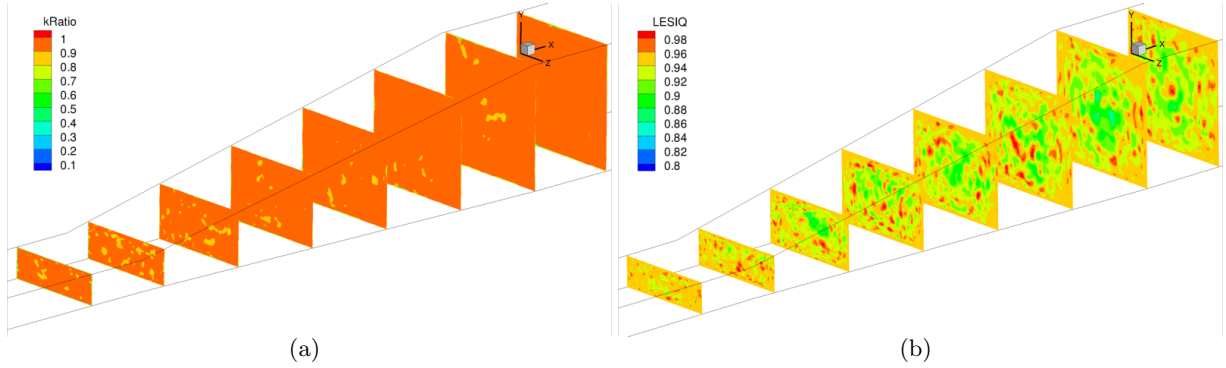
Figure 3.11   The quality of the LES assessed using the metric of (a) Ratio of resolved to total Turbulent kinetic energy and (b) LES_IQ_ν parameter

While the overall quality of the flow was assessed to be of good quality, a validation exercise is required for the flow variables predicted using this simulation.

3.2.1   Verification

The numerical stability of the LES was ensured by maintaining a CFL number less that 1, which required a time step of $\Delta t \sim 10^{-5}$s. The flow is initialized by random fluctuations and is allowed to develop for about $27\tau_{ave}$ (flow throughs based on average bulk velocity in diffuser). The averaging is later started and continued for $70\tau_{ave}$, which was required to converge the mean and second-moments of flow velocity. The actual averaging required differed from diffuser-to-diffuser. Notably, Diffuser 2 of Cherry et al. (2008) required about $100\tau_{ave}$ to converge the statistics.

With the availability of DNS data of Ohlsson et al. (2010) a more detailed comparison of flow variables has been made. The mean streamwise velocity and the dominant Reynolds stress

$\overline{uu}$ show a good agreement with DNS data as in Figure 3.12. Separation is formed towards the double-sloped corner and midway through the diffuser it spreads across the whole top wall. The LES predicts the top wall separation to be farther downstream than DNS; the volume of separation is also under predicted. The results presented here use a sharp-edged diffuser inlet, while the DNS used a filleted edge. A bulk of the turbulent kinetic energy comes from the streamwise normal stress $\overline{uu}$, and the values compare quite well. A high normal stress is predicted at the sloped edges at inlet, than by DNS this is caused due to the high shear introduced by the sharp edge. Downstream of the diffuser, the magnitudes and trends of $\overline{uu}$ agree well.

(a) $\overline{u}/u_{bulk}$

(b) $100u_{rms}/u_{bulk}$
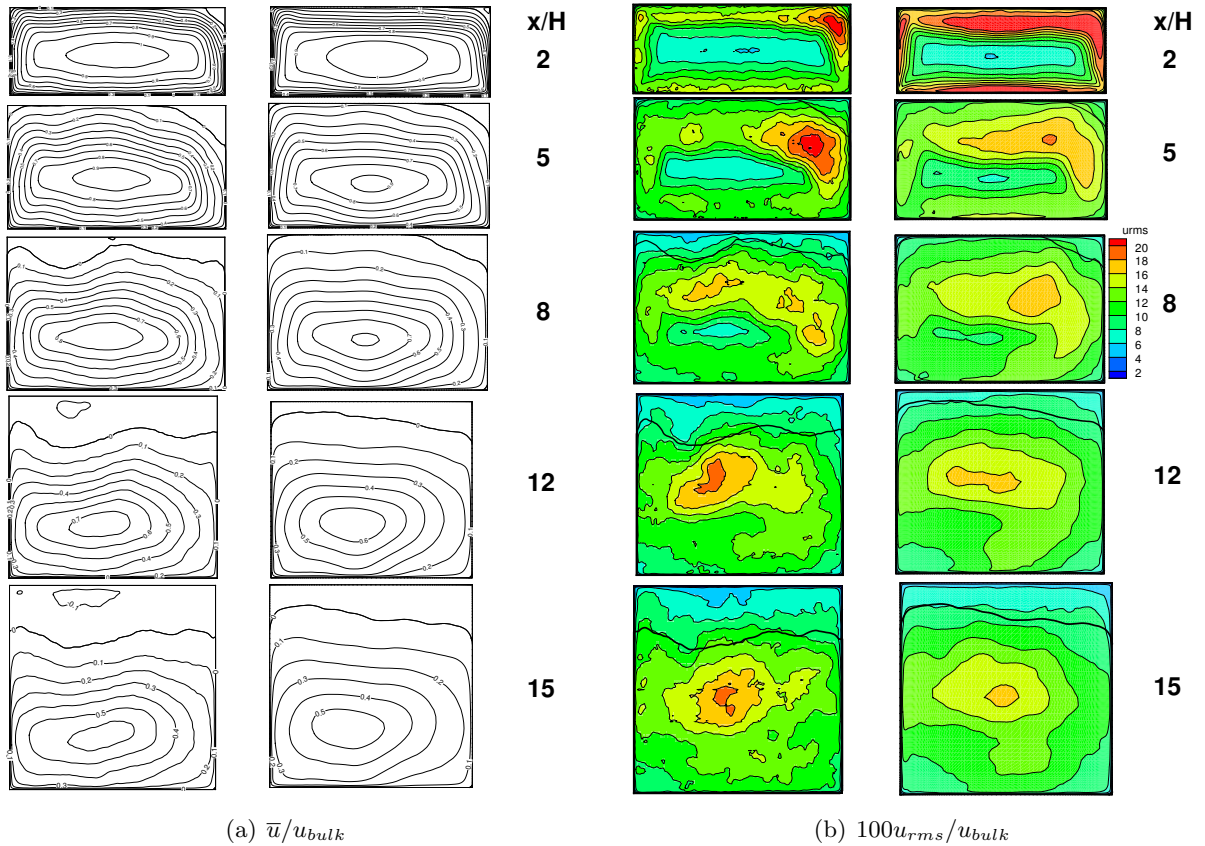
Figure 3.12   Contour lines of mean streamwise velocity and streamwise RMS velocity at various transverse planes. The DNS is to the left and LES on the right on each of Figures (a) and (b). Each line is spaced by 0.1 and the zero velocity line is bold.

A detailed comparison of separation predicted at different transverse planes is made. Figure

3.13 compares the mean flow velocities and normal and shear stress quantities in the mid-plane of the diffuser with DNS. Comparisons at other z-planes close to the asymmetric wall and the parallel wall showed a similar good agreement, and are shown in Figures 3.14 - 3.16. The spike in all the Reynolds stress is observed close to the diffuser inlet. This is only a local effect due to the geometric difference and the flow develops downstream, giving a better comparison to DNS. Near the bottom wall the velocity gradients are steep and have been captured by the dynamic LES model. Resolving this gradient is critical to predicting the wall pressure coefficient C_p accurately. At the inlet to the diffuser, the $\overline{u_i u_j}$ profile is similar to that of a fully developed flow in a 2-D channel, with the $\overline{uv}$ changing signs at mid-channel. The effect of the 3-D separation deviates the flow from turbulence equilibrium causing the maximum Reynolds stress to exist close to the centre of channel. In the straight section downstream of diffuser, the flow does not show signs of relaxing to equilibrium from the mean velocity and stress profiles.

The coefficient of pressure C_p in this diffuser is reported on the bottom wall, as the flow is attached along that wall and along any streamwise section there is very little circumferential variation of pressure. The C_p is calculated using the pressure at the diffuser inlet and the bulk velocity at that location. Good agreement with experiments is shown in Figure 3.17. The wall pressure follows the effects of separation manifesting as blocked cross-sectional flow area. Data show a rapid rise in C_p near the inlet of the diffuser, followed by a gradual reduction in the pressure gradient until the trend becomes nearly linear at about x/L=0.7. At this point, the reverse flow region has spread almost uniformly across the top expanding wall. The pressure profile contains an inflection point at about x/L=0.4, where separation is still at the sloped corner. The pressure curve shows no change of slope at x/L=0.53, the position where the separation bubble leaps across the top expanding wall of the baseline diffuser. Near the inlet, the flow area expands rapidly and the separation bubble is small, resulting in a large expansion of the potential flow area, hence a large pressure gradient. Farther downstream (0.2 < x/L < 1), the separated region grows rapidly and somewhat counteracts the growing cross-sectional area of the diffuser by reducing area for forward flow. This results in a more gentle pressure gradient. Downstream fo the diffuser outlet (x/L > 1) the flow reattaches recovering additional pressure.

3.2.2   Diffuser series

The series of diffusers simulated using LES show separation to switch to the side wall at about $\mathcal{R}$3. As noticed in Figure 3.18 the volume of separated flow reduces as $\mathcal{R}$increases, which improves the efficiency of the diffuser as the wall pressure recovery reaches a maximum of 80% for $\mathcal{R}$> 2. The secondary flow are similar, each case having 4 major vortices located at diffuser exit(x/H=15) transverse section. Figure 3.19 shows the vortex cores to be located away from the reverse flow region, but towards the corners. In a sense, the major streamwise vortices are displaced by the reverse flow region.
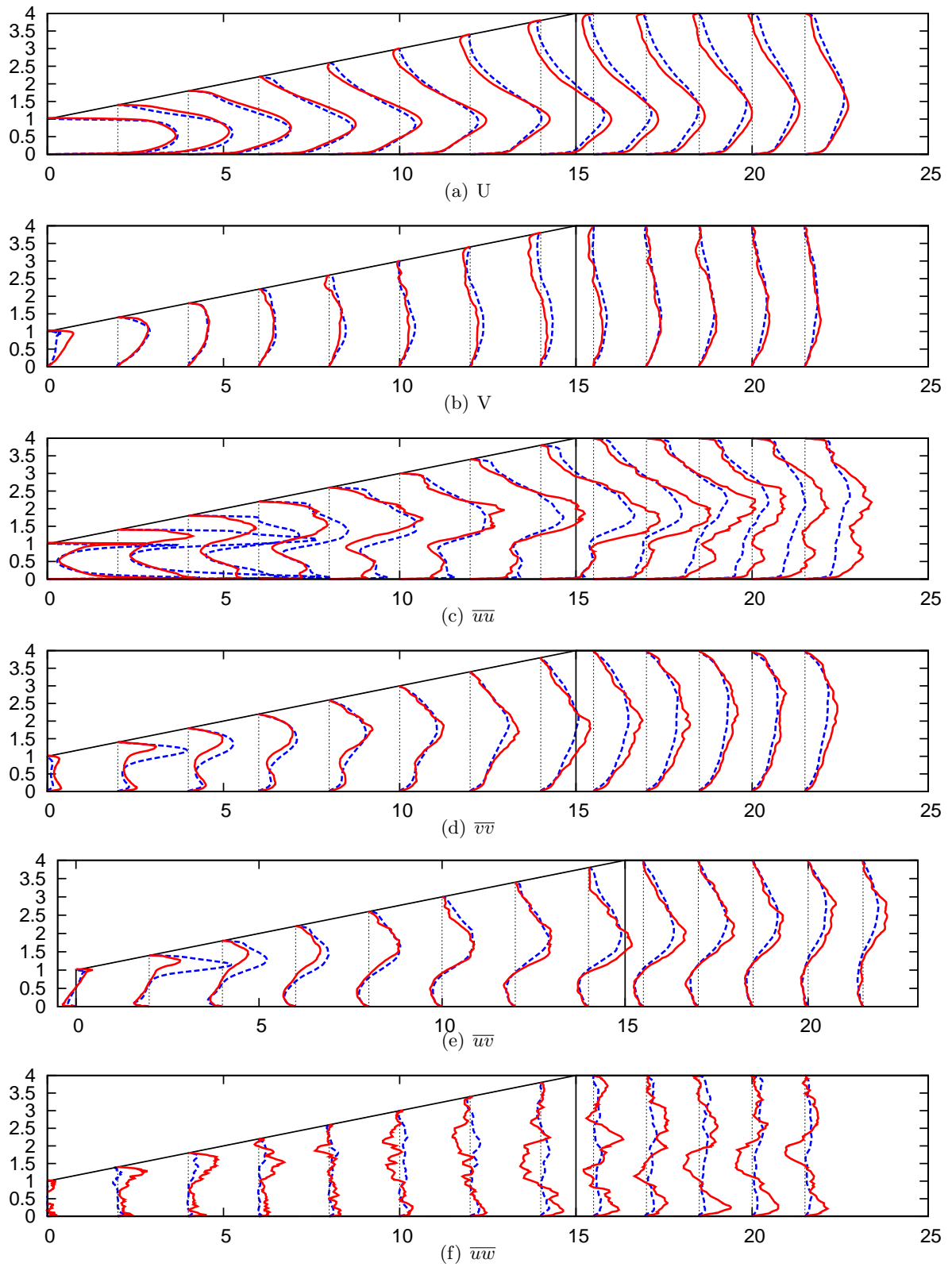
Figure 3.13   Comparison of mean flow velocities, resolved kinetic energy, and Reynolds stresses along **z/B=1/2** by LES of baseline diffuser. DNS are solid and LES are dashed.
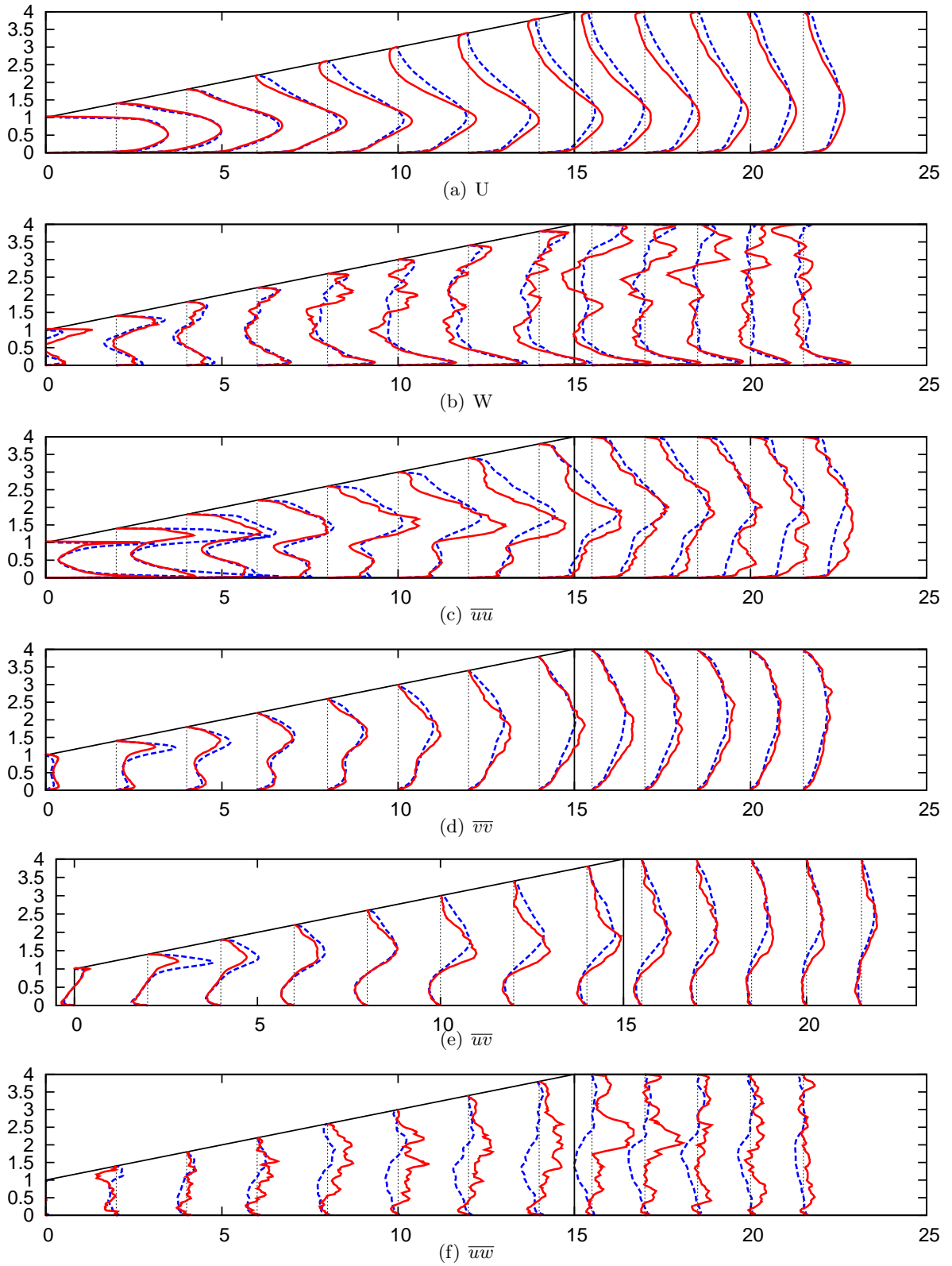
Figure 3.14   Comparison of mean flow velocities, resolved kinetic energy, and Reynolds stresses along **z/B=1/4** by LES of baseline diffuser. DNS are solid and LES are dashed.
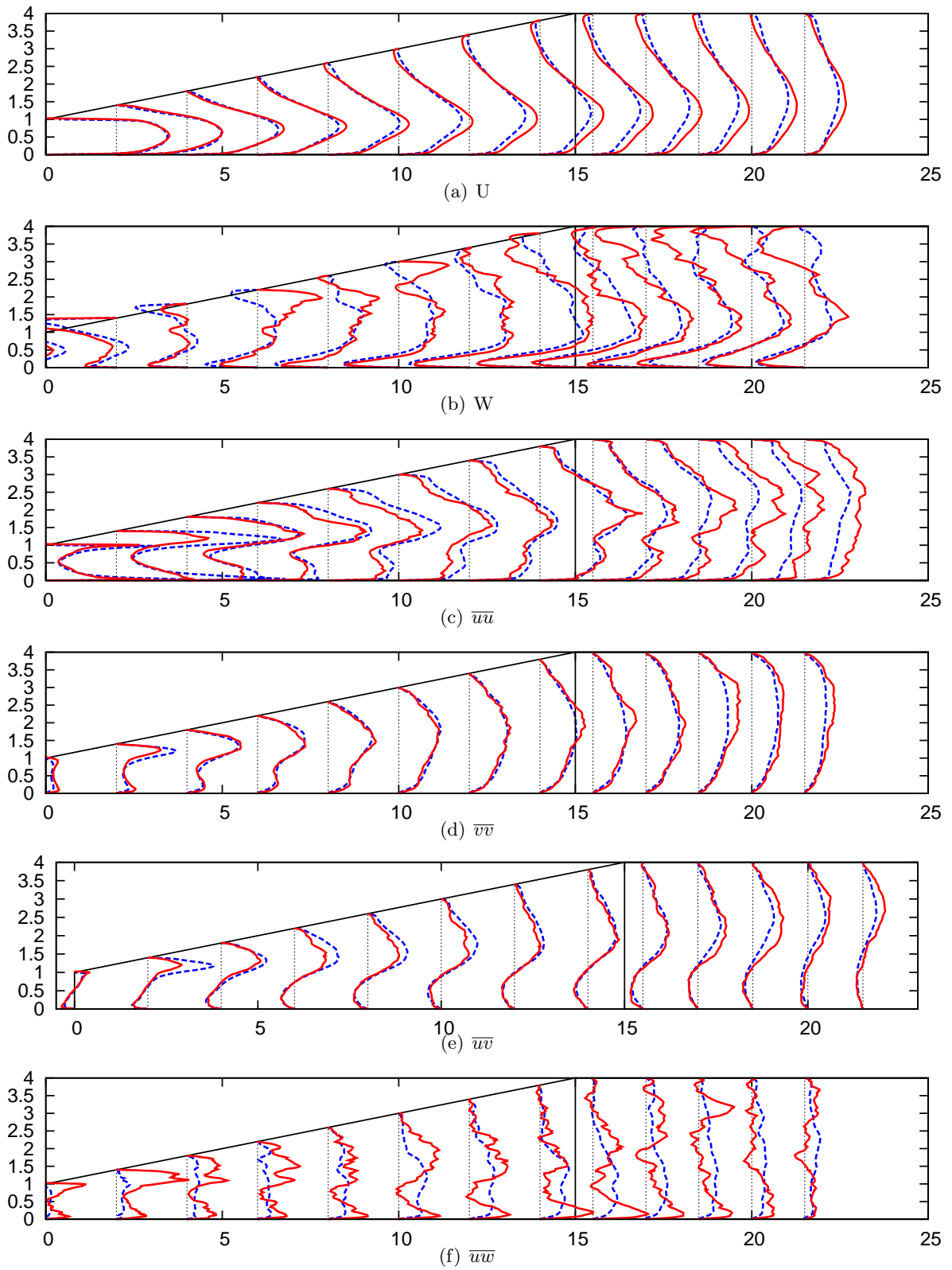
Figure 3.15   Comparison of mean flow velocities, resolved kinetic energy, and Reynolds stresses along **z/B=3/4** by LES of baseline diffuser. DNS are solid and LES are dashed.
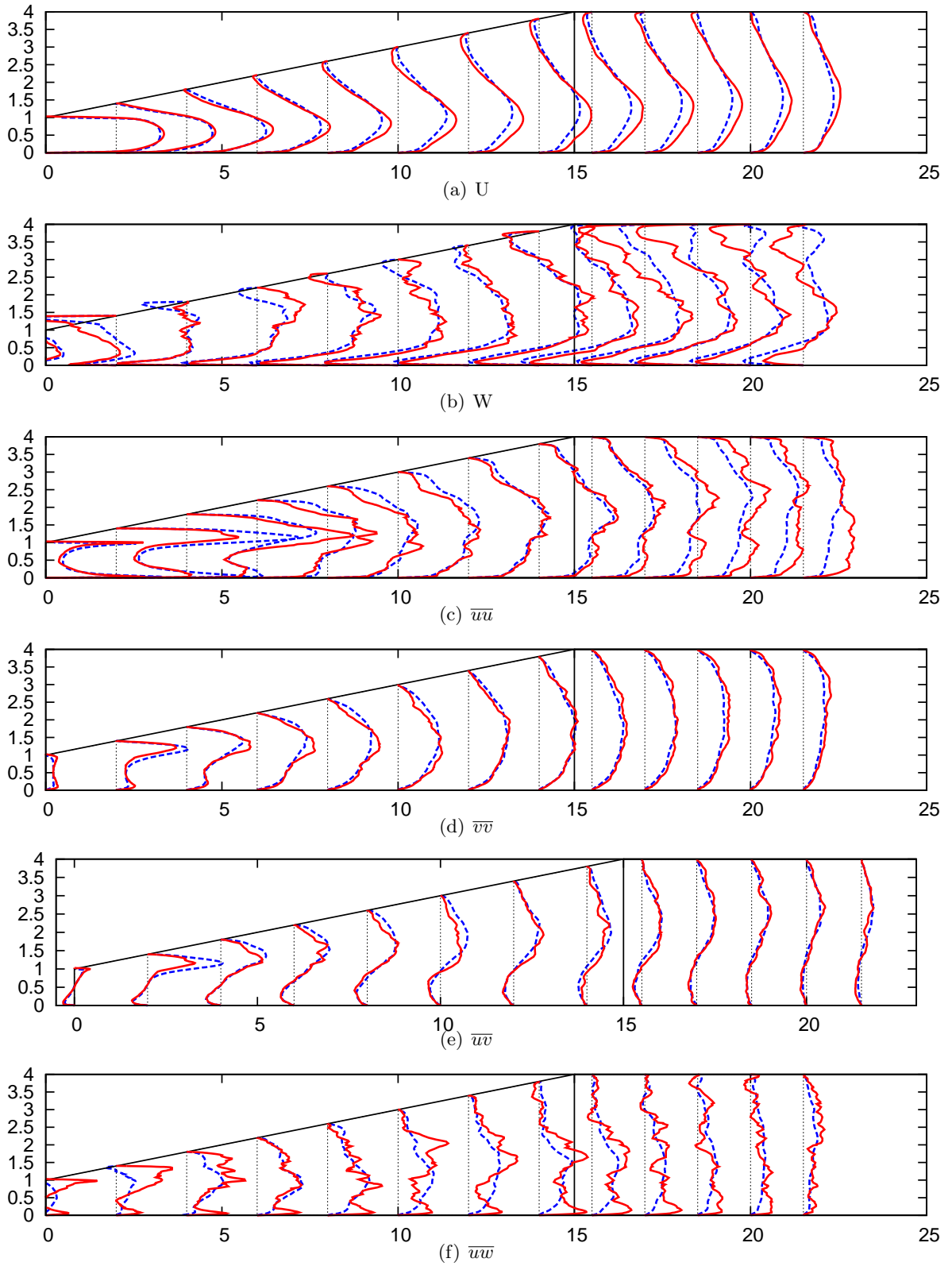
Figure 3.16   Comparison of mean flow velocities, resolved kinetic energy, and Reynolds stresses along **z/B=7/8** by LES of baseline diffuser. DNS are solid and LES are dashed.
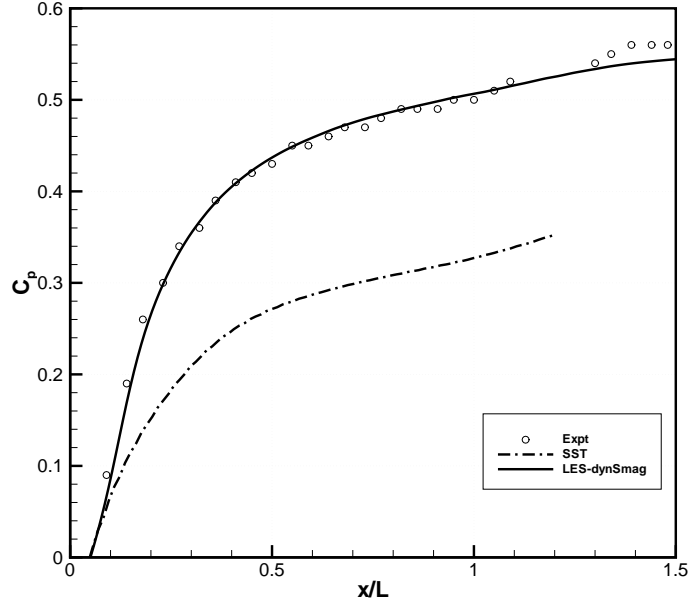
Figure 3.17 Coefficient of pressure $\left(C_p = \frac{p - p_{ref}}{0.5\rho U_{bulk}^2}\right)$ variation along the bottom wall of base-line diffuser predicted by LES, x/L is the non-dimensional diffuser length. The experimental C_p has been shifted by -0.02 to provide a better comparison.

| (a) $\mathcal{R}1$ | (b) $\mathcal{R}2$ | (c) $\mathcal{R}3$ |
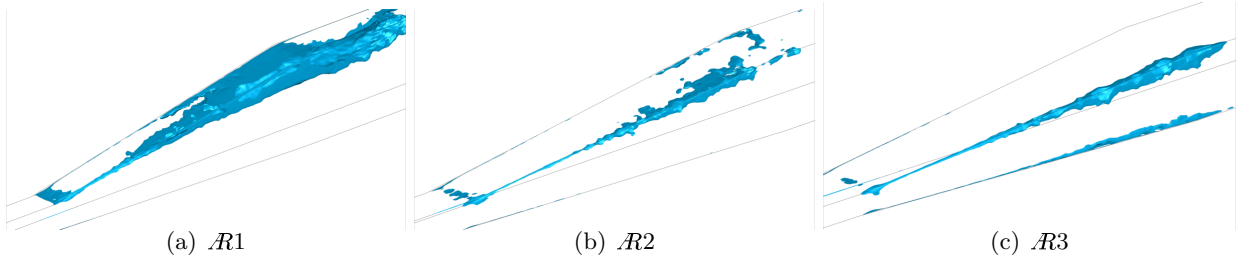
Figure 3.18 Separation surface predicted by LES for the diffuser series

3.3   Comparison of LES and DES

The motivation for using the DES was due to the reduced grid requirement than an LES. The former provided a qualitative comparison with experiments, however a good quantitative comparison is paramount to generate data needed for turbulence model development. The SAS predicts a larger separation (Figure 3.20) than LES and separation spreads over the whole top wall ahead of the streamwise location shown in experiments. The wall C_p predictions are much lower due to the higher flow blockage. Similar observations of low C_p and larger separation are observed by SAS simulations of Uribe et al. (2010) and hybrid LES-RANS of Abe and Ohtsuka
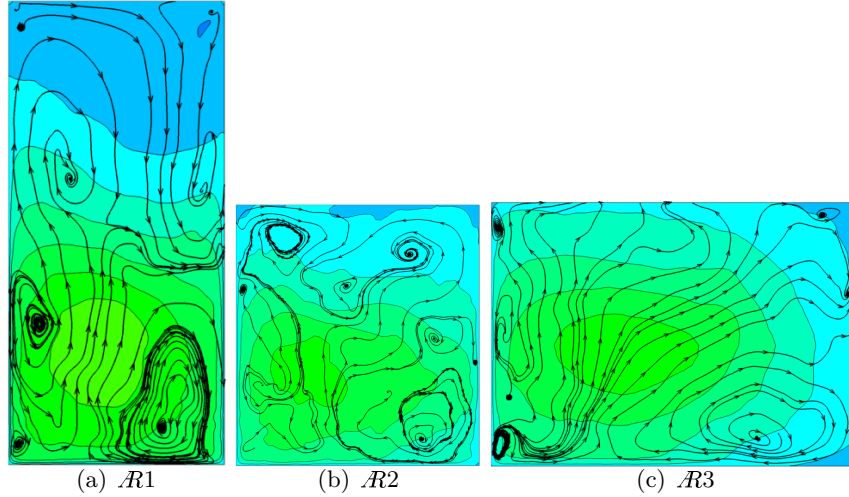
Figure 3.19   Secondary flow predicted by LES at the diffuser exit plane x/H=15 of the diffuser series. The cross-sections are shown in different scale, in real the areas are same.

(2010). The main reason for the inaccuracy of the DES arises from the inability of the near wall RANS, $k - \omega$ SST model in the SAS to predict Reynolds stress anisotropy that occur in the corner flow of diffuser. This will be the subject of discussion in the next chapter.

The LES have been computationally intensive both in grid requirement and numerical solution, however the flow predict compare well with DNS. The Reynolds stress budget terms $(\mathcal{P}_{ij}, \epsilon_{ij}, \Pi_{ij}, D_{ij})$ are accurate and can be used for model development.
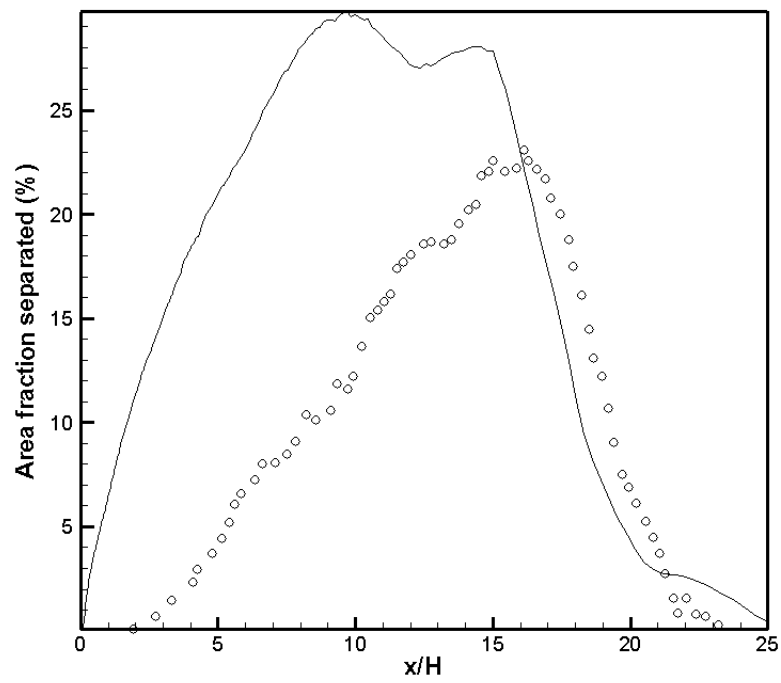
Figure 3.20   Fraction of cross-sectional area separated predicted by DES and Experiments for the baseline diffuser

CHAPTER 4.   SINGLE POINT CLOSURE MODELS

Turbulence modeling has been focused on single-point correlations for their tractability. The cost of this assumption is that the whole spectrum of turbulence scales cannot be resolved as possible by multi-point correlations. Statistical approach as Reynolds averaging is required to simplify the analysis of Navier-Stokes equations, as given by the RANS equations in (4.1). The mean is represented as $\overline{U} = U$ and fluctuation $\overline{u} = 0$.

$$\partial_t U_i + U_j \partial_j U_i = -\frac{1}{\rho} \partial_i P + \nu \nabla^2 U_i - \boldsymbol{\partial_j \overline{u_j u_i}} \tag{4.1}$$

$$\partial_i U_i = 0$$

The Reynolds stress tensor (bold in 4.1) is unknown and needs the solution of second-moment transport equations. Higher (n+1) moment terms occur in a n-moment equation, which lead to the closure problem. Most engineering turbulence models solve for first-moment equations(4.1) with a model for the stress term. The Boussinesq assumption is widely used to close the RANS equation.

$$-\overline{u_i u_j} = 2\nu_T S_{ij} - \frac{2}{3} k \delta_{ij} \tag{4.2}$$

In two-equation models, $\nu_T = C_\mu \frac{k^2}{\epsilon} = \frac{k}{\omega}$ the former for the $k - \epsilon$ model and the later for $k - \omega$ model. The algebraic expression in 4.2 has been successful in predicting a variety of flows. However in complex flows with separation, streamline curvature, frame rotation, stagnating flows, etc the Boussinesq assumption fails.

4.1   Linear eddy-viscosity models (LEVM)

A linear relation between Turbulent stress and mean-flow strain limits the ability to model few flow effects. The stress anisotropy is defined as $a_{ij} = \frac{\overline{u_i u_j}}{k} - \frac{2}{3} \delta_{ij}$, where $k = \frac{1}{2} \overline{u_i u_i}$. Hence

one can analyse the departures from isotopy ($a_{ij} = 0$) by looking at the 5 distinct elements of this symmetric and trace-free matrix. In the eddy viscosity models the anisotropy is a function of strain only, $a_{ij} = -2\nu_T S_{ij}$. Due to this assumption the following are the drawbacks:

- Normal stress anisotropy is not accounted.

- Only accurate for equilibrium flows

- No streamline curvature effects included, as $a_{ij} = \mathcal{F}_{ij}(S_{ij})$

As mentioned earlier, secondary normal stress anisotropy ($\overline{v^2} \neq \overline{w^2}$) is required to predicting secondary flow of second-kind. At the vicinity of stagnation point, the primary-secondary stress anisotropy ($\overline{u^2} \neq \overline{v^2}$) needs to be resolved to predict the correct turbulence production and hence kinetic energy. This was corrected by limiter on the turbulence timescale by Durbin (1996).

The model coefficients are most determined from idealized flow conditions, such as homogeneous shear and plane shear flow. The deviation of the flow from turbulence equilibrium is measured by the ratio of Production-to-dissipation $\mathcal{P}/\varepsilon$. Where;

$$\mathcal{P}_{ij} = -\overline{u_i u_k}\frac{\partial U_j}{\partial x_k} - \overline{u_j u_k}\frac{\partial U_i}{\partial x_k}; \qquad \varepsilon_{ij} = \frac{2}{3}\varepsilon\delta_{ij}$$
$$\implies \frac{\mathcal{P}}{\varepsilon} = -\overline{u_l u_k}\frac{\partial U_l}{\partial x_k}\frac{1}{\varepsilon} = -a_{ij}\left(\frac{S_{ij}k}{\varepsilon}\right)$$

In plane shear flow $\mathcal{P}/\varepsilon = -a_{12}d_y U(k/\varepsilon)$ and hence the accuracy of predicting the ratio is only dependent on modeling fidelity of Reynolds shear stress. Most models are calibrated based on this flow $\frac{-\overline{uv}}{k} = \sqrt{C_\mu}(= 0.3)$. In two-dimensional APG and separated flows, this fails, leading to over prediction of eddy-viscosity. Menter (1994) introduced a stress limiter redefining ν_T.

4.1.1 Anomalies in predicting 3-D separation

Three-dimensional separation is nearly independent of the Reynolds number and is characterized by two adjacent boundary layers subjected to APG. The modeling challenges are rooted in the complexity of the strain and vorticity field. To predict separation in asymmetric diffusers the model has to resolve the complex 3-D flow, lateral straining, stramline curvature, streamwise vorticity, secondary flow of second kind, and effect of transverse pressure gradient.

All LEVM fail to resolve these complex flow physics. The models that have been tested are $k - \epsilon$, $k - \omega$ SST,$k - \omega$, Spalart-Allmaras and $v^2 - f$. The LEVM predominantly used is the $k - \omega$ SST of Menter (1994). The primary and secondary flow predicted in the baseline diffuser are shown in Figure 4.1. The primary flow is formed initially along the top, but later switches to the side sloped wall. The flow predicted at the first section in 4.1(b) compares well with the SAS, both the primary and secondary flow with vortices and singular points. However downstream SST predicts the vortices to dissipate faster and separation is formed on the wrong wall. A similar primary flow separation is predicted by the tested LEVM. The $v^2 - f$ predicts the near-wall anisotropy accurately, however fails to predict the separation on the top wall, due to the three-dimensional nature of the flow separation. A modified implementation of this model, the $\zeta - f$ was tested by Ryon (2008) to produce the same error.

(a)   (b)
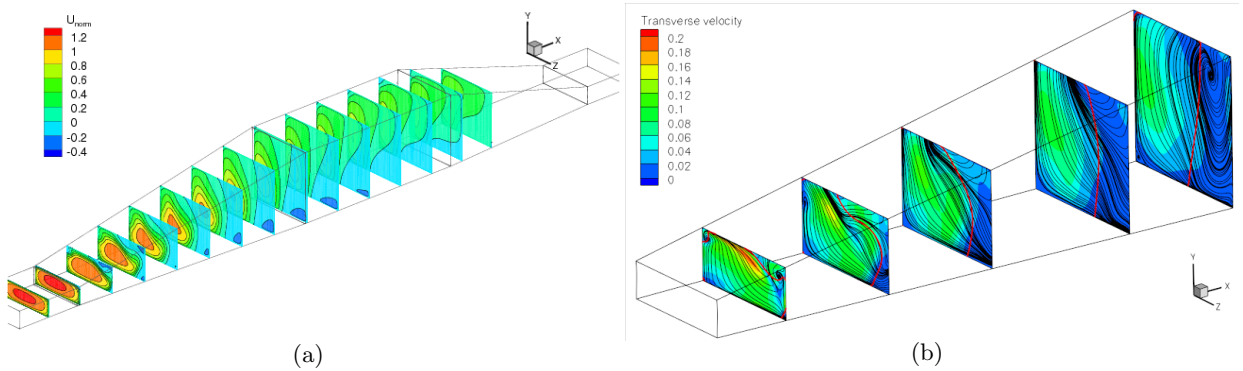
Figure 4.1   Primary and secondary flow predicted using the $k - \omega$ SST model. The transverse velocity in (b) is normalized by U_{bulk}

Flow separation in the diffuser series predicted by SST indicate a switching of separation from top to side wall at about $Æ$2. However eddy-resolving simulations predict the switch to happen at $Æ$2.5. The SST model responds to the increase in $Æ$much faster than LES, thus are oversensitive to minor transverse pressure. Qualitatively a correct separation is predicted by RANS for the rest of $Æ$series, but the separation volume is high and hence streamwise velocities increase leading to a lower wall pressure coefficient predicted than by the LES.

In diffuser configurations, the SST model showed sensitivity to minor changes in geometry. Few are;

(a) $\mathcal{R}1$ (b) $\mathcal{R}1.5$

(c) $\mathcal{R}2$ (d) $\mathcal{R}2.5$
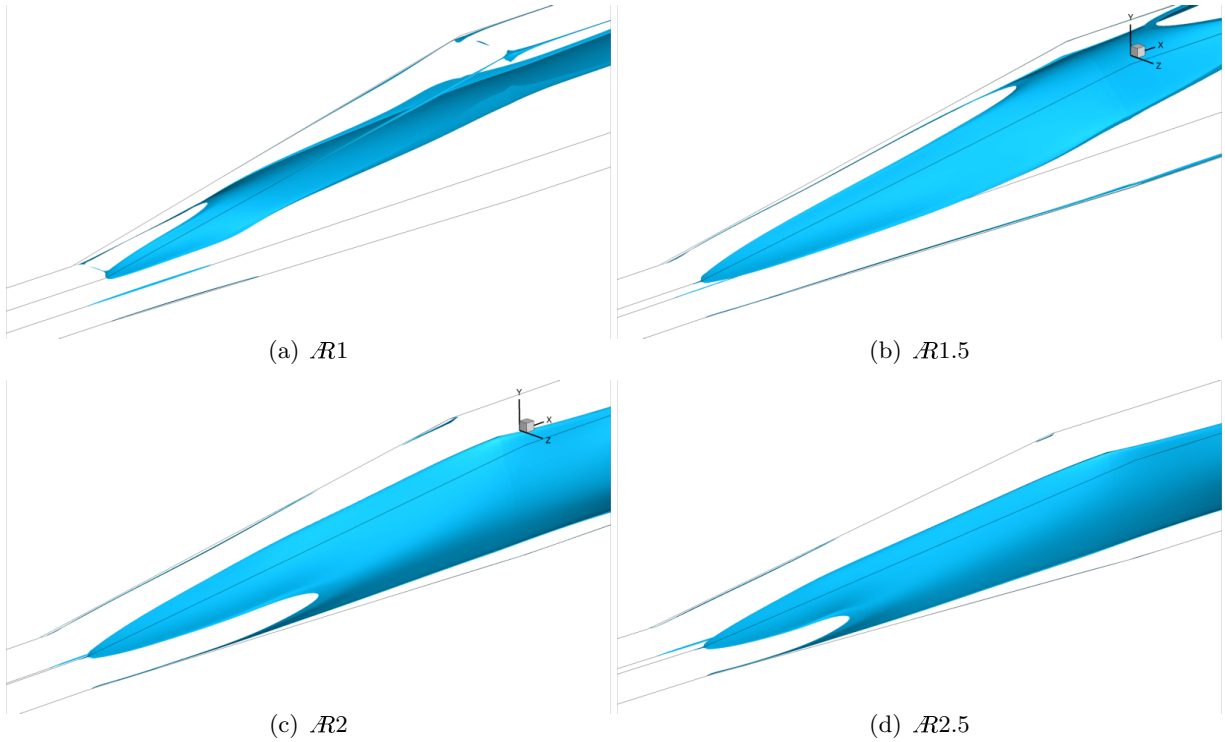
Figure 4.2 Separation surface predicted by SST model in the series of diffusers.

Side slope angle asymmetry

On the diffuser with sloping on one of the transverse direction only, the model predicts separation on the sloped top wall. However even with an infinitesimal slope $(0.02\,\mathrm{deg})$, the separation surface moves to the small-sloped side. This diffuser has the same $\mathcal{R}=3.33$ of the baseline. The physics of flow predicted by SAS shows the separation on the top wall. In the top-only sloped geometry the area expansion increases linearly with x, and so is the streamwise pressure gradient. However the introduction of secondary slope make the area expansion rate with x quadratic and dp/dx follows the trend. This corroborates with the earlier observation that the SST model is highly sensitive to transverse pressure gradients.

Higher symmetric side slope

A series of diffusers with a constant top slope and inlet $\mathcal{R}$is created, the side walls are flared symmetrically with different angles. As the side slope angles increase, the dp/dx gets

steeper close to the diffuser inlet. At lower symmetric side slopes the separation is formed on the top wall, but at about 2.5 deg the separation becomes asymmetric (Figure 4.3). The separation happens on either the left or right symmetric side, depending on the way the flow was initialized, in a sense bistable.

(a) 1 deg   (b) 2.56 deg
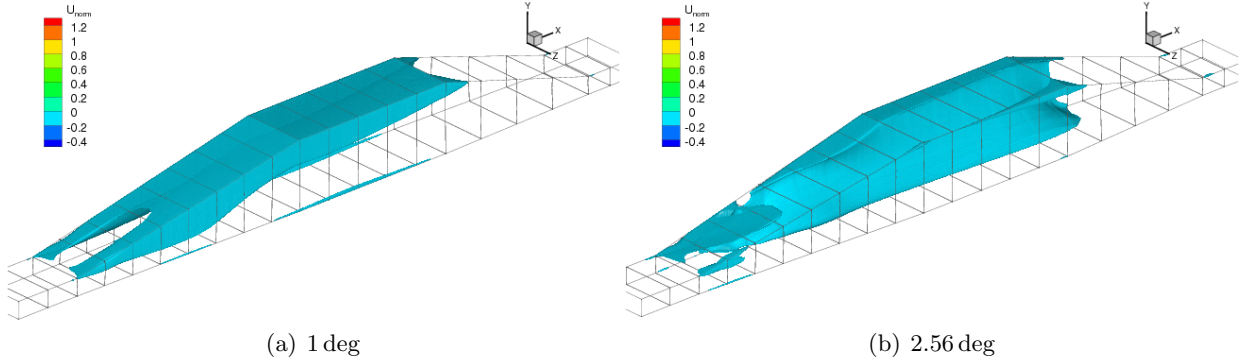
Figure 4.3   Anomalous separation surface predicted by SST in diffusers with symmetric side slope angles.

Flow predicting by DES did not indicate an asymmetric flow at 2.56 deg, but a total separation on the top wall. The Reynolds stress model of SSG showed a similar separation, but of smaller reverse flow. The Spalart-Allmaras model predicted a symmetric side wall separation at all angles. Hence there is a disparity in predictions among RANS models for this series, however incorrect. The SST model destabilize in predicting separation at high streamwise pressure gradients.

4.2   Sensitizing C_μ to flow separation

The $C_\mu = 0.09$ is calibrated for 2-D mild shear flows. Hence sensitizing the coefficient to general 3-D shear flows would make the model accurate to predict flow separation. The effect of increasing C_μ in the standard $k-\omega$ SST model causes separation to decrease in the Obi et al. (1993) diffuser (Figure 4.4). The increase in the coefficient's value leads to a direct increase in eddy-viscosity which causes more dissipation and hence a smaller separation. As complex flows are composed of a variety of fundamental flow physics, having C_μ change locally based on the flow velocity would be required to resolve the local flow. Some of the modeling parameters are

explored.
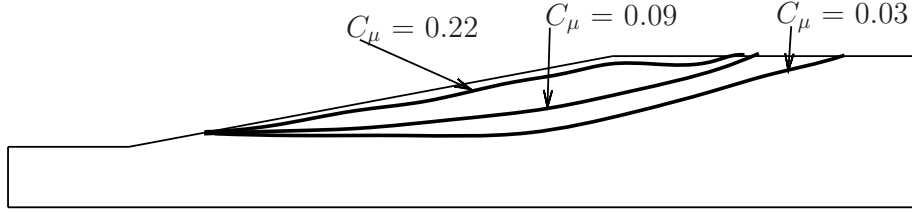
Figure 4.4   Sensitivity of 2-D diffuser flow separation to variations in C_μ value. The separation line is in bold.

4.2.1   Modeling parameters

The modeling parameter for 3-D separation should satisfy these requirements, values should vanish in 2-D flow, show proper sensitivity to the real physics of separation, and computationally inexpensive. Galilean invariance is required to have the model applicable in moving inertial frames. The velocity gradient tensor $(\partial_j U_i)$ has been largely used as a flow visualization tool (Haimes and Kenwright, 1999), however recently studies have indicated the time evolution of this tensor to resolve turbulence dynamics. The velocity gradient tensor can be decomposed into a symmetric and antisymmetric part and into its Eigen values.

$$\partial_j U_i = S_{ij} + \Omega_{ij} = \begin{pmatrix} U_x & U_y & U_z \\ V_x & V_y & V_z \\ W_x & W_y & W_z \end{pmatrix} = \begin{pmatrix} \lambda_1 & 0 & 0 \\ 0 & \lambda_2 & 0 \\ 0 & 0 & \lambda_3 \end{pmatrix}$$

The Eigen values reduce the number of variables to characterize the flow based on the local velocity gradient. Three Eigen values($\lambda_1, \lambda_{2r} + i\lambda_{2i}, \lambda_{2r} - i\lambda_{2i}$) have one real and a complex conjugate pair, except at critical points where all three values are real and distinct. Critical point theory has been used by Haimes and Kenwright (1999) to classify the local flow condition based on the distribution of λ_i in the Argand plane. The distribution of the λ_i shown in Figure 4.5, shows the SAS to have a much wider scatter along the real axis than the SST prediction. Based on the classification of Haimes and Kenwright (1999), points on the positive Real(λ_i) are accelerating and decelerating on the -ve direction. The flows is also spiraling out if the points are in the I and IV quadrant and spiraling in if the the II and III quadrant. Hence the SAS

predicts more accelerated spiraling flow than the SST, which corroborates with observation that eddy simulations resolve multiple vortices in the diffuser. On the contrary SST predicts a few high spiraling flow, as the vortices are dissipated. The field of λ_i in diffuser did not isolate the regions of separation in the SST simulation, hence would not be a suitable variable for making C_μ dependent on.

(a) SST   (b) SAS
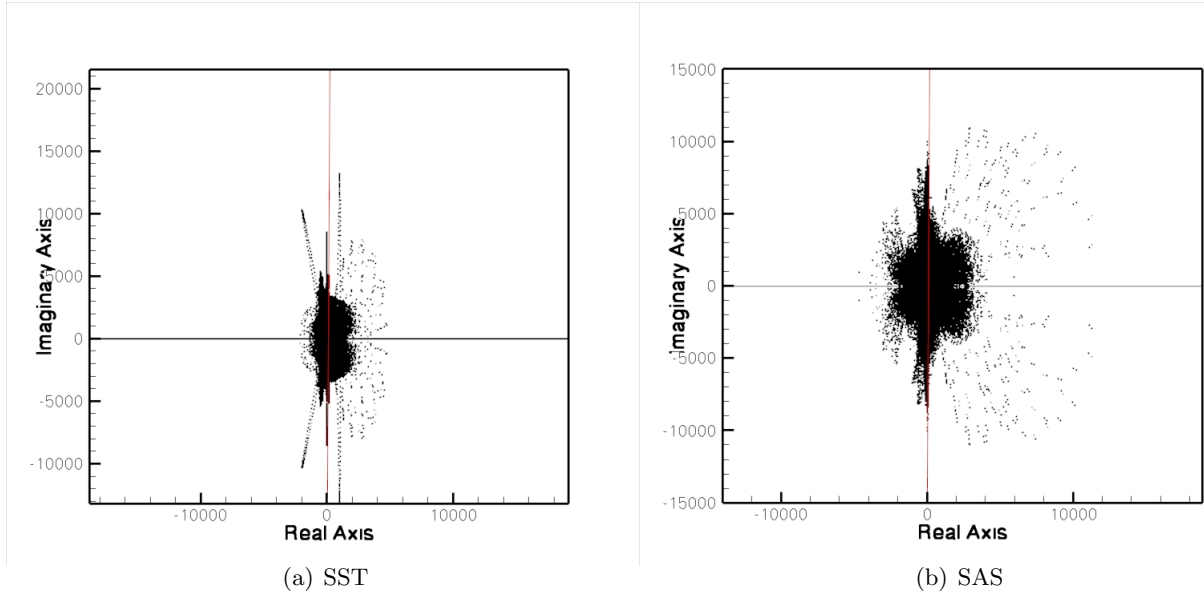
Figure 4.5   Scatter of Eigen values of Velocity gradient tensor predicted by SST and SAS models for the baseline diffuser.

Helicity

Helicity$(U \cdot (\nabla \times U))$ is a fundamental flow kinematic variable which relates to linkages of vortex lines in flow. In plane channel flow, helicity is generated by $-\overline{uv}$. LEVM are only sensitized to strain and hence including this term could improve modeling fidelity. The parameter computed using the SST model does not isolate the regions of separation (Figure 4.6), as the flow does not contain streamwise vortices by the time the separation spreads along the side wall. In the SAS flow field, the parameter identifies the various streamwise vortices. It is notworthy, that no vortices are observed in the separated region along the top wall. Helicity would serve as a post-processing variable, but not as a dynamic variable to model eddy-viscosity.
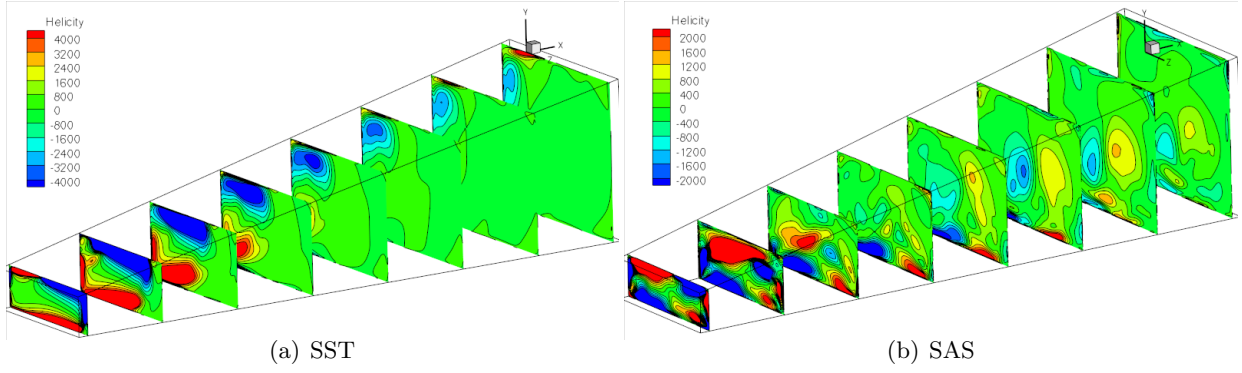
Figure 4.6   Contours of Helicity in transverse plane of baseline diffuser predicted by SST and SAS models

WALE parameter

Nicoud and Ducros (1999) proposed a sub-grid model term that uses the velocity-gradient tensor to estimate the turbulence dissipation at the sub-grid level. The term is designed to predict the near-wall scaling correctly, hence needs both strain and vorticity tensor, as shown below.

$$\frac{(\mathcal{S}_{ij}^d \mathcal{S}_{ij}^d)^{3/2}}{(\overline{S}_{ij}\overline{S}_{ij})^{5/2} + (\mathcal{S}_{ij}^d \mathcal{S}_{ij}^d)^{5/4}} \qquad \text{where, } \mathcal{S}_{ij}^d = \frac{1}{2}\left((\partial_j U_i)^2 + (\partial_i U_j)^2\right) - \frac{1}{2}\delta_{ij}(\partial_k U_k)^2$$

Larger values are observed in the high strain regions close to the diffuser, but the separated regions along the side wall are not distinguished (Fig. 4.7).
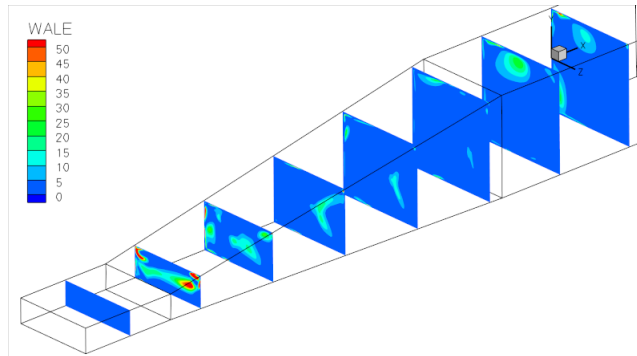
Figure 4.7   WALE parameter evaluated using SST-predicted flow field of baseline diffuser.

4.3   Importance of Anisotropy

The LEVM failure in predicting 3-D separation is mainly caused due to the inability to adequately represent anisotropy. Analysis of the DNS data of Ohlsson et al. (2010) provides insight into the anisotropy in the baseline diffuser. Lumley(1977) was the first to study the turbulence anisotropy by a plot of second($II_a = a_{ik}a_{ki}$) and third ($III_a = a_{ik}a_{kl}a_{li}$) invariants. The realizable values of anisotropy are bounded by a triangle, with the lower two sides caused due to axisymmetric contraction/expansion and the upper by 2-component turbulence (near-wall). For example, the stress at x/H=0.5 along mid-plane of diffuser is shown in Fig. 4.8b. It is observed that the dominant stress are the diagonal terms. At this section, the trends of stress are similar to that in a 2-D channel. **a** is computed for all points along this spanwise line and along all lines in the mid-plane (z/B=0.5). This is shown in Fig. 4.9a, we notice that most of the anisotropy is due to axisymmetric expansion, which is expected. Also it is noticed that a bulk of the flow is close to isotropy, the highest anisotropy is fed from inlet (cyan line, x2) and it reduces as the flow moves downstream. The flow anisotropy is characterized by axisymmetric expansion near the inlet, but downstream (x/H >12) it becomes close to axisymmetric contraction. The shift in anisotropy from expansion to contraction is quicker as the flow moves downstream diffuser close to the side-sloped wall.

Local information on the nature of anistropy can be studied from the plot Fig. 4.10. Here we notice again that the flow is farthest from isotropy at the inlet, as II_a and III_a reach their global maximum. In each of the profiles, we also notice that the local maxima is towards the walls, and another maxima appears mid-span as the flow develops downstream. The II_a has a smaller value in the top separated wall relative to the bottom, the III_a in this region is much higher in this separated region than the bottom wall. Hence the turbulence in the separated region undergoes an axisymmetric contraction.

4.4   Anisotropy-resolving models

The model that can represent anisotropy realistically with its dynamics would be the differential Reynolds Stress Model (RSM). However these models need appropriate wall treatment
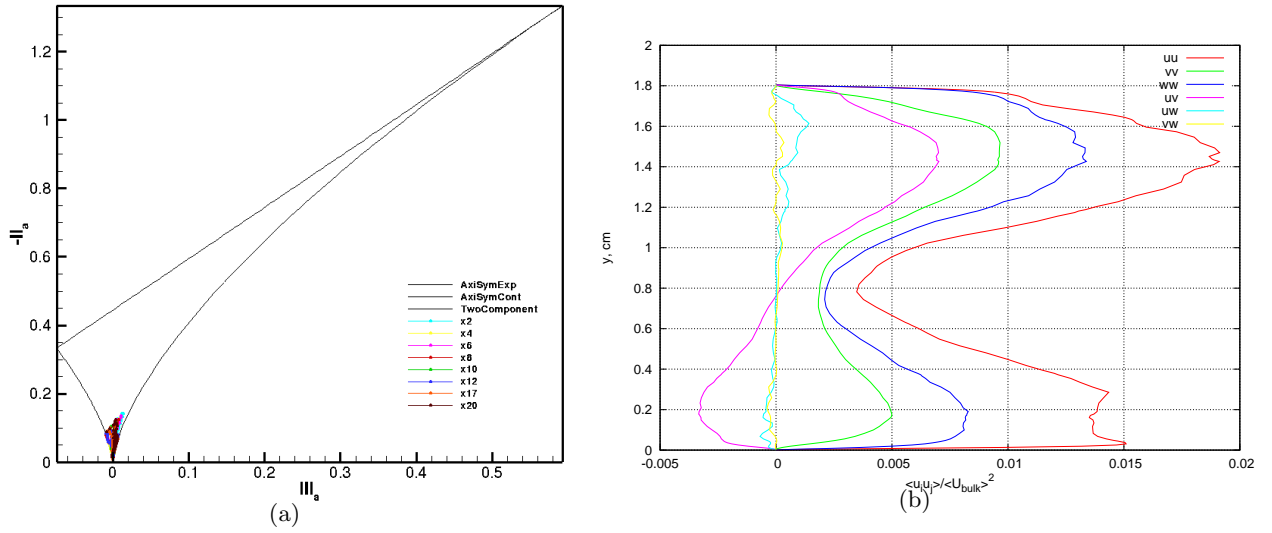
Figure 4.8   DNS data reported for a_{ij} (a) Lumley invariant map for flow anistropy along mid-plane of diffuser z/B=0.5(b) The complete Reynolds stress tensor $\overline{u_i u_j}$ plotted at x/H=4 at diffuser midplane (z/B=0.5)
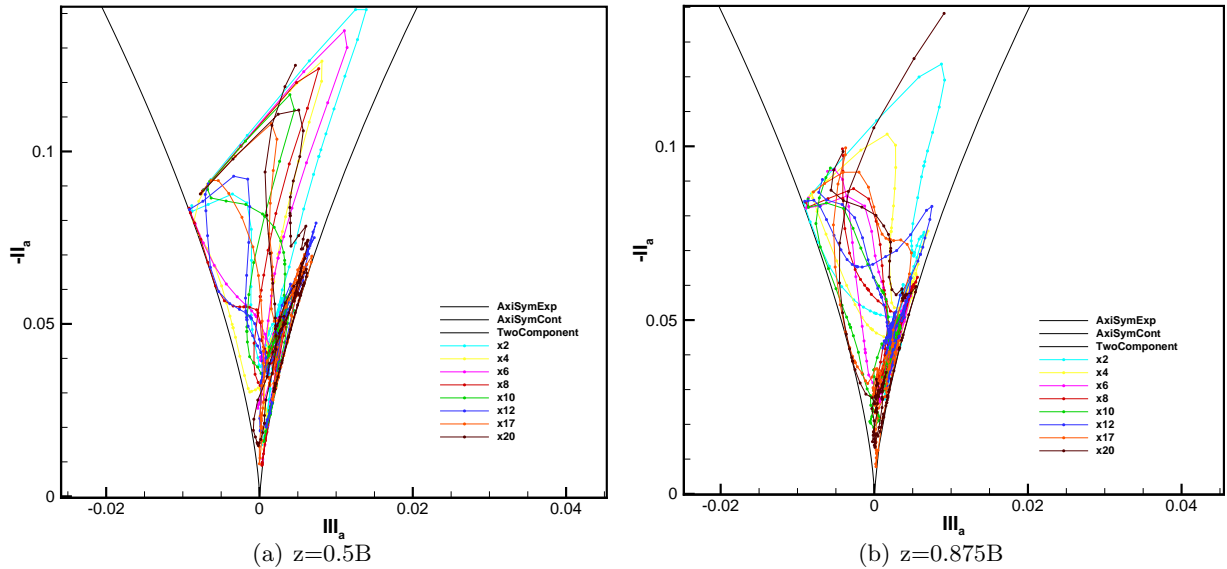
Figure 4.9   A plot of a_{ij} invariants at various streamwise locations (x/H) from DNS results
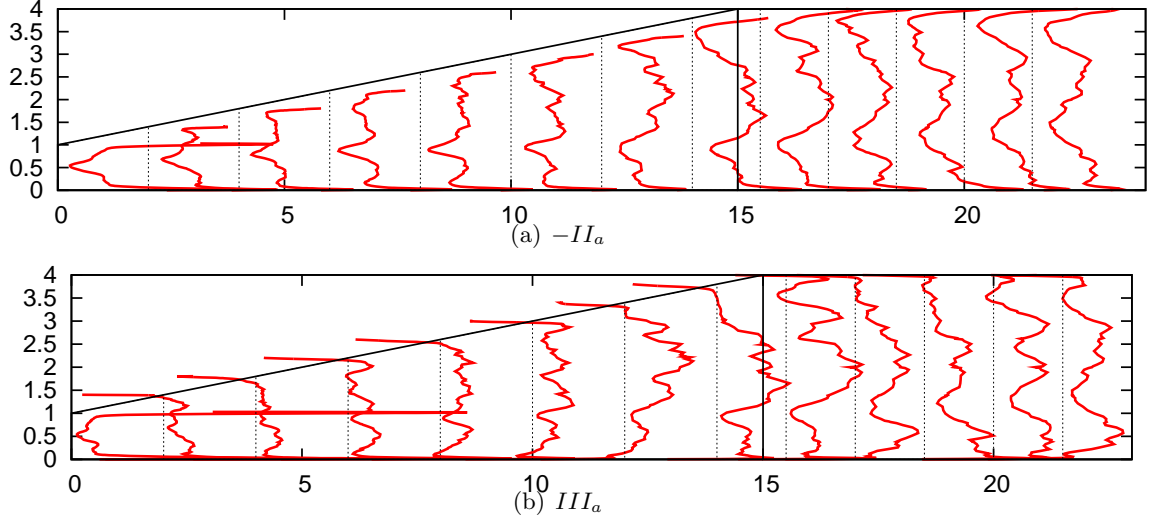
Figure 4.10   Variation of Reynolds stress anisotropy(a_{ij}) invariants along the span of the base-
line diffuser midplane (z=0.5B) from DNS results

and have numerical difficulties with convergence. For 3-D diffuser flows, the RSM under pre-
dict separation. The model used for the pressure-strain term Π_{ij} is the source of error, the
linear model by Launder et al. (1975) provide a better comparison with experiments than the
quadratic model of Speziale et al. (1991). The solution to the full RSM equation is:

$$K\frac{\mathcal{D}a_{ij}}{\mathcal{D}t} - \text{Diff}_{ij}^{(a)} = -\frac{\overline{u_i u_j}}{K}(\mathcal{P} - \varepsilon) + \mathcal{P}_{ij} - \varepsilon_{ij} + \Pi_{ij} + \varepsilon C_{ij}^a \tag{4.3}$$

The above 6 equations need to be solved with the mean flow equations 4.1. The turbulent
length and time scale is determined by solving the standard K and ε equations together. The
$\text{Diff}_{ij}^{(a)}$ lumps together the diffusion terms of Reynolds stress$(\partial_k \overline{u_i u_j u_k})$ and turbulent kinetic
energy. Pressure strain correlation $\mathcal{P}_{ij}$ and dissipation rate tensor ε_{ij} need modelling, while
the other terms can be directly evaluated from the Reynolds stress tensor.

The Algebraic Reynolds stress equation was first proposed by Rodi (1972), where the Diffu-
sive terms were neglected and each component in $\overline{u_i u_j}$ changes in time with the same rate as its
trace. The later assumption is well known as the moving or weak equilibrium, $(\frac{\mathcal{D}}{\mathcal{D}t}\left(\frac{\overline{u_i u_j}}{K}\right) = 0)$,
which implies $\mathcal{D}_t a_{ij} = 0$. Equation 4.3 reduces to this form.

$$\frac{\overline{u_i u_j}}{K}(\mathcal{P} - \varepsilon) = \mathcal{P}_{ij} - \varepsilon_{ij} + \Pi_{ij} + \varepsilon C_{ij}^a \tag{4.4}$$

This is an implicit relation between the Reynolds stresses and the mean velocity gradient field that replaces the Boussinesq hypothesis (4.2). The pressure-strain term is modeled separately by a slow and a rapid part. The slow part is not affected by mean flow gradients and refers to return to isotropy of homogeneous turbulence. Rotta(1975) modeled is term as $\Pi_{ij}^s = -c_1 \varepsilon a_{ij}$. The rapid part is modeled using a generalized model. Few of the models for Π_{ij}^r that are considered are: Launder Reece Rodi(1975):

$$\frac{\Pi_{ij}^r}{\varepsilon} = \frac{4}{5}\mathbf{S} + \frac{9c_2 + 6}{11}(\mathbf{aS} + \mathbf{Sa} - \frac{2}{3}\{\mathbf{aS}\}\mathbf{I}) + \frac{7c_2 - 10}{11}(\mathbf{a\Omega} - \mathbf{\Omega a}) \tag{4.5}$$

Speziale, Sarkar & Gatski(1991):

$$\begin{aligned}
\frac{\Pi_{ij}}{\varepsilon} &= -\left(\frac{C_1}{2} + \frac{C_1^*}{2}\frac{\mathcal{P}}{\varepsilon}\mathbf{a}\right) + \left(C_3 - \frac{C_3^*}{2}\sqrt{II_a}\right)\mathbf{S} + \frac{C_4}{2}(\mathbf{aS} + \mathbf{Sa} - \frac{2}{3}\{\mathbf{aS}\}\mathbf{I}) \\
&\quad - \frac{C_5}{2}(\mathbf{a\Omega} - \mathbf{\Omega a}) + \frac{C_2}{4}(\mathbf{a^2} - \frac{1}{3}II_a\mathbf{I})
\end{aligned} \tag{4.6}$$

Bold fonts are used to refer to tensors and to the trace. For simplicity, the LRR model has been chosen by Wallin and Johansson (2000) with a $c_2 = \frac{5}{9}$. Representing the velocity gradient tensor($\partial_j U_i = \mathbf{S} + \mathbf{\Omega}$) by the symmetric strain and anti-symmetric vorticity tensor has advantages, in a rotating reference frame only Ω need to be corrected, secondly, manipulation of symmetric tensor is much convenient. The Coriolis contribution C_{ij}^a is only considered in rotating flows. Substituting terms into Equation 4.4 gives the algebraic RSM in terms of stress anisotropy:

$$\left(c_1 - 1 + \frac{\mathcal{P}}{\varepsilon}\right)\mathbf{a} = -\frac{8}{15}\mathbf{S} + \frac{7c_2 + 1}{11}(\mathbf{a\Omega} - \mathbf{\Omega a}) - \frac{5 - 9c_2}{11}(\mathbf{aS} + \mathbf{Sa} - \frac{2}{3}\{\mathbf{aS}\}\mathbf{I}) \tag{4.7}$$

This equation is nonlinear in $\mathbf{a}$ since $\mathcal{P}/\varepsilon \equiv -\{\mathbf{aS}\}$. The last term drops out when considering $c_2 = \frac{5}{9}$ rather than using 0.4 as originally proposed by Launder et al. (1975). The effect of this simplification by assuming c_2 on flow separation is described later. Solving Eq. 5.1 is computationally cumbersome since there is no diffusion or damping present.

4.5 Explicit Algebraic Reynolds Stress Model(EARSM)

The difficulty with solving for Equation 5.1 is the treatment of the implicit term $\mathcal{P}/\varepsilon$. Pioneering work was done by Pope (1975) where an exact solution for 2-D flows was derived

by treating $\mathcal{P}/\varepsilon$ implicitly. Taulbee (1992) and Gatski and Speziale (1993) have solved the equation by assuming $\mathcal{P}/\varepsilon$ to be constant. An explicit solution has been derived by Wallin and Johansson (2000) by assuming coefficients on the LHS of 5.1 to be constant and later solving for $\mathcal{P}/\varepsilon$. The systematic generalization presented explains the development of the model from the first principles of tensor consistency and the assumptions are clear; making it straight-forward to propose modeling refinements. This makes the model more attractive than Non-linear eddy-viscosity model where phenomenological methods are used. Some of the pros and cons of the model are:

+ Accounts for normal stress anisotropy

+ For rotating flows, material frame difference can be included by correcting $\boldsymbol{\Omega}$

- Streamline curvature and Coriolis contributions need to be included via. $\boldsymbol{\Omega}$

- only accurate for equilibrium flows

- Anisotropy is only sustained by local velocity gradients.

- Dynamics of stress anisotropy not included.

4.5.1 Formulation

In general, any isotropic tensor $\mathbf{a}$ which is a function of two isotropic tensors $\mathbf{S}$ and $\boldsymbol{\Omega}$ can be expressed as a tensorial polynomial, composed of basis terms up to order 5. Using Cayley-Hamilton theorem (Pope, 1975) the constitutive relation for $\mathbf{a}$ can be derived to be as:

$$
\begin{aligned}
\mathbf{a} = &\underline{\beta_1 \mathbf{S}} + \beta_2 \left(\mathbf{S}^2 - \frac{1}{3} II_s \mathbf{I} \right) + \beta_3 (\boldsymbol{\Omega}^2 - \frac{1}{3} II_\Omega \mathbf{I}) + \underline{\beta_4 (\mathbf{S}\boldsymbol{\Omega} - \boldsymbol{\Omega}\mathbf{S})} \\
&+ \beta_5 (\mathbf{S}^2 \boldsymbol{\Omega} - \boldsymbol{\Omega}\mathbf{S}^2) + \beta_6 (\mathbf{S}\boldsymbol{\Omega}^2 + \boldsymbol{\Omega}^2 \mathbf{S} - \frac{2}{3} IV \mathbf{I}) + \beta_7 (\mathbf{S}^2 \boldsymbol{\Omega}^2 + \boldsymbol{\Omega}^2 \mathbf{S}^2 - \frac{2}{3} V \mathbf{I}) \\
&+ \beta_8 (\mathbf{S}\boldsymbol{\Omega}\mathbf{S}^2 - \mathbf{S}^2 \boldsymbol{\Omega}\mathbf{S}) + \beta_9 (\boldsymbol{\Omega}\mathbf{S}\boldsymbol{\Omega}^2 - \boldsymbol{\Omega}^2 \mathbf{S}\boldsymbol{\Omega}) + \beta_{10} (\boldsymbol{\Omega}\mathbf{S}^2 \boldsymbol{\Omega}^2 - \boldsymbol{\Omega}^2 \mathbf{S}^2 \boldsymbol{\Omega})
\end{aligned} \tag{4.8}
$$

The invariants of the velocity gradient are $II_s = \{\mathbf{S}^2\}, II_\Omega = \{\boldsymbol{\Omega}^2\}, IV = \{\mathbf{S}\boldsymbol{\Omega}^2\}, V = \{\mathbf{S}^2 \boldsymbol{\Omega}^2\}$. Here the stain and vorticity tensors are non-dimensionalized by the turbulence timescale K/ε. Upon substitution of Equation 4.8 in 5.1, the β coefficients can be solved for explicitly in terms of $N = \left(c_1 - 1 + \frac{\mathcal{P}}{\varepsilon} \right)$. Once the β coefficients are evaluated they can be substituted back into 5.1, which simplifies into a polynomial equation.

In 2-D flows the anisotropy tensor basis reduces to the underlined terms in 4.8 and the N equation is a cubic polynomial. In 3D flows, $\beta_{1,3,4,6,9}$ are non-zero and N is a 6-order polynomial. The EARSM can be thought as a correction to eddy viscosity ($\beta_1 = -2C_\mu$) in RANS models. In 2D mean flows only two invariants matter II_S and II_Ω, the other invariants IV=0 and $V = \frac{II_S II_\Omega}{2}$.

4.5.2 Implementation and Numerics

A variant of this model, the baseline EARSM (BEARSM) developed by Menter et al. (2009) has been implemented in OpenFOAM. The advantage of using this model is there is no near-wall damping required, as it solves the $k - \omega$ equation in the boundary layer. The simulations conducted has a $y_+ = 2$, hence wall integration is performed. To handle generic near wall grids, an automatic wall function has been used, the details are described in Menter and Esch (2001).

The tensor polynomial used in BEARSM is given below;

$$
\begin{aligned}
\mathbf{a} =& \beta_1 \mathbf{S} + \beta_3 (\mathbf{\Omega}^2 - \frac{1}{3} II_\Omega \mathbf{I}) + \beta_4 (\mathbf{S\Omega} - \mathbf{\Omega S}) + \beta_6 (\mathbf{S\Omega^2} + \mathbf{\Omega^2 S} - \frac{2}{3} IV\mathbf{I} - \boxed{II_\Omega \mathbf{S}}) \\
&+ \beta_9 (\mathbf{\Omega S\Omega^2} - \mathbf{\Omega^2 S\Omega} - \boxed{\frac{1}{2} II_\Omega (\mathbf{S\Omega} - \mathbf{\Omega S})})
\end{aligned}
\tag{4.9}
$$

The tensor basis described in Wallin and Johansson (2000) has only 5 basis terms considered, the simplification from the full 10 terms to 5 is due to the simplified Algebraic RSM that uses the LRR pressure-strain model with $c_2 = 5/9$. The same 5 tensor basis terms are used by Menter et al. (2009), however with additional terms boxed in Equation 4.9. This essentially means that the β's evaluated using WJ and Menter's decomposition would be different, however the $\mathbf{a}$ would be same as the tensor basis are identical. This implies the fully consistent solution of $\mathcal{P}/\varepsilon$ is a solution to N^6 polynomial, same as WJ. For simplicity, the root of N^3 has been used for 3-D flow simulations. At a given $\mathbf{S}$ and $\mathbf{\Omega}$, the root of N^3 was only 4% lower than the root of N^6 polynomial being sought.

The code allowed for symbolic operations on tensor algebra, hence simplifying the implementation. The eddy-viscosity is computed as $\nu_T = K/\omega$. A production limiter as in 4.10 is used in k- and ω- equation. From simulations, it is noticed that the production is lower than

10 times dissipation and the limiter is unused.

$$P_k = \min\left(-\overline{u_i u_j}\partial_j U_i, 10 C_\mu K \omega\right) \tag{4.10}$$

The discretization of the dissipative term in RANS Eq. 4.1 is performed as $\partial_j \left[\nu\partial_j U_i - \overline{u_j u_i}\right]$ rather than $\partial_j \left[\nu\partial_j U_i\right] - \partial_j \left[\overline{u_j u_i}\right]$. Evaluating the divergence of the former proved less stiff than the other and amenable to convergence. The BEARSM were initialized with a converged SST flow field and RMS residuals reduced by 8 orders. As the model relies on accurate evaluation of the mean flow velocity gradients to compute anisotropy, the accuracy of the divergence scheme affects the quality of predictions. The following are the two solver numerics that were used;

upwind • Gauss Seidel smoother

- Gradient scheme e.g. $\nabla p=$ Gauss linear (2-order accurate)

- Divergence scheme e.g.$\overline{U}\cdot\nabla(U) =$ Gauss upwind. (1-order accurate) similarly for K & ω

- $\nabla\cdot\overline{u_i u_j} =$ Gauss linear

- Laplacian schemes e.g. $\nabla\cdot(\nu_{Eff}\nabla\overline{U}) =$ Gauss linear corrected (same for K & ω)

- pressure solver is GAMG with Gauss Seidel smoother

linear Divergence scheme e.g. $\overline{U}\cdot\nabla(U) =$ Gauss linear. (2-order accurate) similarly for K & ω

The linear scheme was used for most of the simulations, but for few diffuser series cases, an upwind convergence was only achievable.

4.5.3   Diffuser flow prediction

Simulation of the baseline diffuser using BEARSM predicts separation on the top wall. The mapped inlet boundary condition was used to generate the fully-developed turbulent flow profile. The profile compares well with the differential RSM predictions.

4.5.4   Mean flow comparison

The mean flow in Figure 4.11 show a good comparison of flow separation at various sections of the diffuser. The separation by the BEARSM is larger than DNS, however it spreads over the top wall at the same location x/H=6. The model sustains a larger core flow velocity, mainly due to the absence of relaxation effects on eddy-viscosity. As the flow is away from equilibrium in the diffuser, this assumption makes the mean flow field to respond immediately to changes in local anisotropy. The secondary flow magnitude and direction are accurately reproduced by the model. There are two vortices at the bottom that stay though the length of the diffuser. A saddle node is present at x/H>5 and stays at the centre of channel, however the 3 foci (vortex core) that converge at this saddle change position relative to the walls. The secondary flow magnitude is only about 5% of the average U_{bulk}. As the flow moves downstream, two vortices close to the top wall approach each other. A closer look of the flow field at the diffuser exit (Fig. 4.12) shows the vortices clearly. The model resolves 3 of the vortices. DNS indicates the vortices to be more closer to the corner than the EARSM.

A modeling simplification was made by considering anisotropy $\mathbf{a}$ to be defined by the 2D tensor basis. This simplifies the calculation, as only $\beta_{1,4}$ terms are used and the fully consistent N^3 is solved to determine $\mathcal{P}/\varepsilon$. This reduced basis is only dependent on two invariant of strain II_s and vorticity II_Ω, the coupled invariants of IV and V are not used due to this 2-D assumption. This velocity flow field is quite different from the 3-D tensor basis as see in Fig.4.12, however topologically correct and an improvement over LEVM. The $\mathbf{S\Omega} - \mathbf{\Omega S}$ tensor term sensitizes the model to 3-D flow effects, though inadequate. The importance of 3-D effects of mean flow on turbulence anisotropy can be visualized by looking at the other three invariants, and their deviation from 2-D effects. Plots of $IV = \mathbf{S\Omega^2}$ in Fig. 4.13a shows the bulk of the flow to have no 3-D effect on anisotropy. Close to the top separated wall, sloped edge and the diffuser core, these effects are dominant. The same is corroborated by visualization of V parameter, a 4th order invariant. Hence in 2-D diffuser results presented, the separation surface predicted is affected by this assumption.

(a) DNS U

(b) DNS VW

(c) EARSM U

(d) EARSM VW
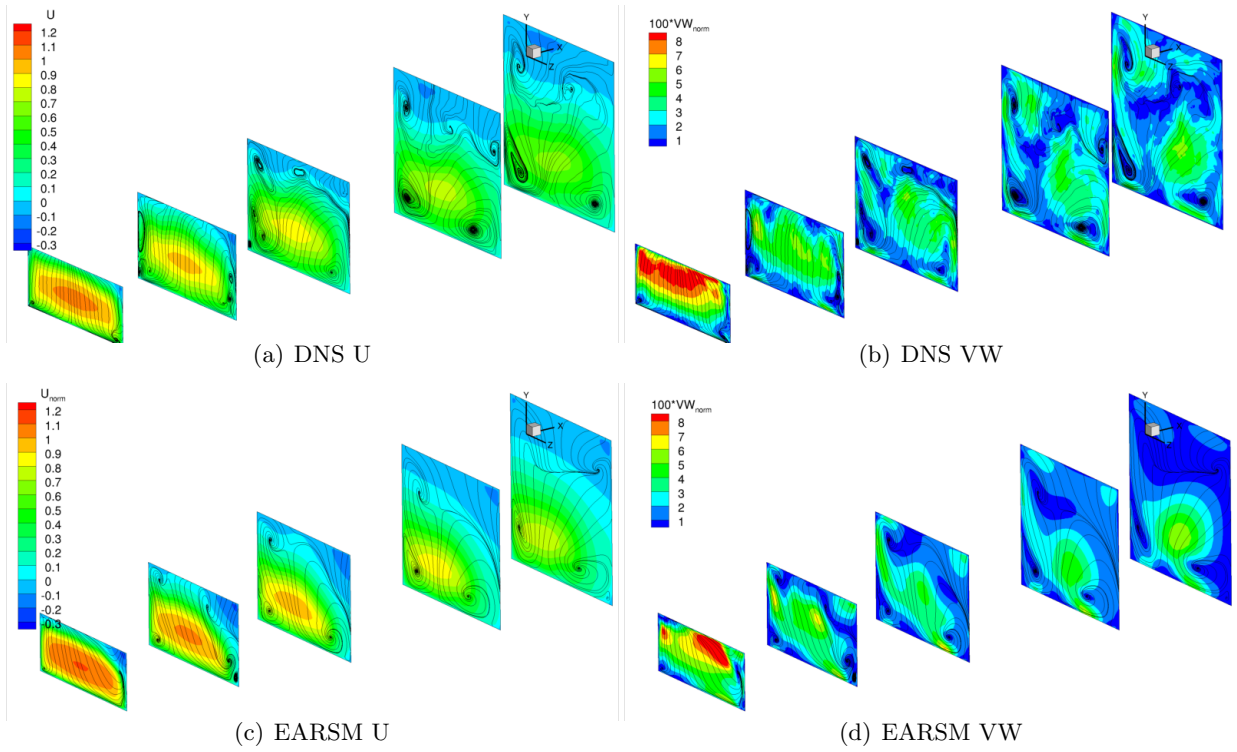
Figure 4.11   Secondary flow predicted by DNS and comparison to BEARSM. The magnitudes of the Mean or secondary flow are colored. The streamlines do not show direction.

DNS

EARSM 3D

EARSM 2D
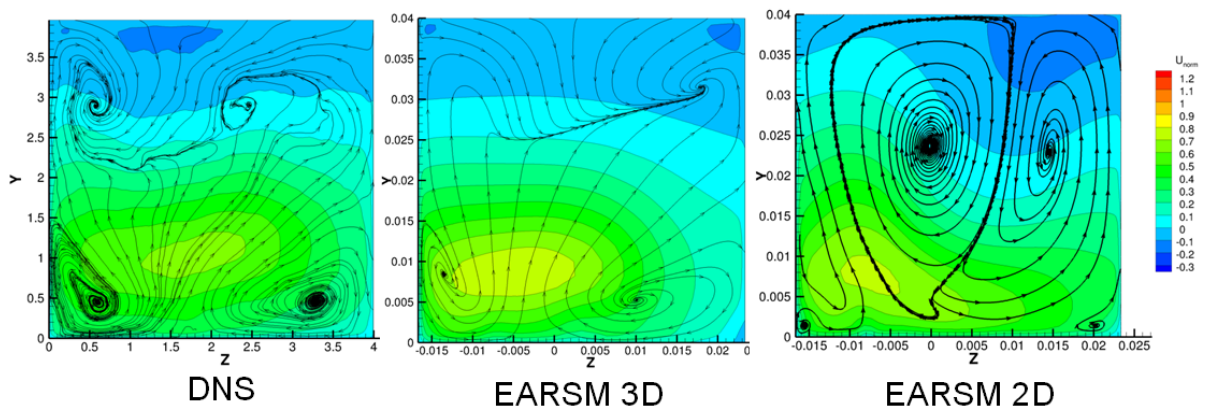
Figure 4.12   Secondary flow predicted by DNS and BEARSM at diffuser exist x/H=15. The flow indicate the presence of 4 vortices.
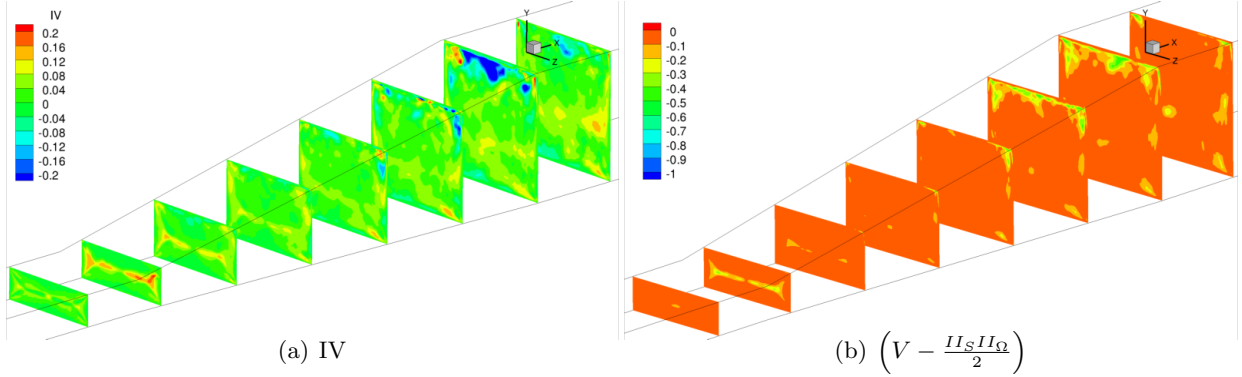
Figure 4.13   Visualization of 3-D flow invariants from LES of baseline diffuser. Regions of 0 have no 3D influence on anisotropy.

4.5.5   Comparison of Reynolds stress

BEARSM predicts the Reynolds stress incorrectly in the diffuser flow, though the gradients of stress $(\overline{v^2} - \overline{w^2})$ and secondary shear stress $\overline{vw}$ are resolved well enough to calculate the accurate momentum sources. As the EARSM is an algebraic model based on local velocity gradient tensors, knowing their values from DNS or LES one could do an *apriori* study on the explicit model's accuracy. However it is noticed that this method is not effective, even for simple corner flows, as the Reynolds stresses are tightly coupled to momentum transport.

4.5.6   Separation in the diffuser family

The sensitivity of the EARSM to transverse pressure gradient are studied using the diffuser series. Separation transitions from top to side wall with increase in $Æ\!R$, as predicted by LES in 4.14. Quantitatively, the model predicts the same trend, with transition at $Æ\!R2.5$. While LES predicts a transition to side wall at $Æ\!R3$. From Figure 4.15 the reverse flow region is predicted to be higher than that of LES. The model is affected by mild transverse pressure gradient, at low $Æ\!R1$ and 1.5, where the separation surface is larger towards the sloped side wall. The diffuser series has a constant streamwise pressure gradient $\partial p/\partial x$, which is much higher than the transverse pressure gradients. The switching of separation is caused due to the gentle interplay of $\partial p/\partial y$ and $\partial p/\partial z$, which affects the lateral straining of turbulence and eventually mean flow. The BEARSM model is able to sustain a higher shear distribution compared to

LES prediction, as the algebraic stress approximation leads to high strain Sk/ε asymptotic limit. The model's oversensitivity to transverse pressure gradients is due to the inaccuracies in the pressure-strain rate model. In this case, it is the LRR. The secondary flow predicted at the diffuser exist resolves the major vortices indicated by LES results

The wall pressure predicted by LES in Fig. 4.16 shows C_p to decrease as Æ increases, which is due to the reduction in separated flow. The EARSM predicts the same trends, however the values are quite low due to the larger reverse flow region. Moreover, the dC_p/dx is steeper at the inlet for LES than in EARSM. The spreading of the separation along the top wall is accurately resolved by the model, as the inflection point in the C_p curves match with that of LES.

4.5.7 General quasi-linear model

A generalized algebraic RSM can be written as:

$$N\mathbf{a} = -A_1 \mathbf{S} + (\mathbf{a\Omega} - \mathbf{\Omega a}) - A_2(\mathbf{aS} + \mathbf{Sa} - \frac{2}{3}\{\mathbf{aS}\}) \tag{4.11}$$

where

$$N = A_3 + A_4 \frac{\mathcal{P}}{\varepsilon}$$

The ARSM is linear in $\mathbf{a}$ and quasi-linear is the sense that terms as $\mathbf{a}\{\mathbf{aS}\}$ can exist. Two models were simulated, the original LRR and linearized SSG, the model coefficients are listed in Table 4.1. The model is computationally intensive as it includes the last term in Eq.4.11 which is neglected in BEARSM. One would expect that with a more complicated formulation for ARSM, the separation predicted would have higher fidelity. However it is observed that separation is predicted only at the corners. The flow predicted is similar to the full RSM results of the corresponding Π_{ij} models. From Fig. 4.17 we notice that the inlet profiles of U_{norm} do not indicate effects of secondary flow that distort the U profiles towards the corners.

4.5.8 Square duct prediction

Simulation of a simpler flow, fully–developed turbulent flow in a square duct was performed to verify the predictability of the EARSM formulation. This case was chosen as secondary

AR 1

AR 1.5

AR 2

AR 2.5

AR 3

BSLEARSM

LES
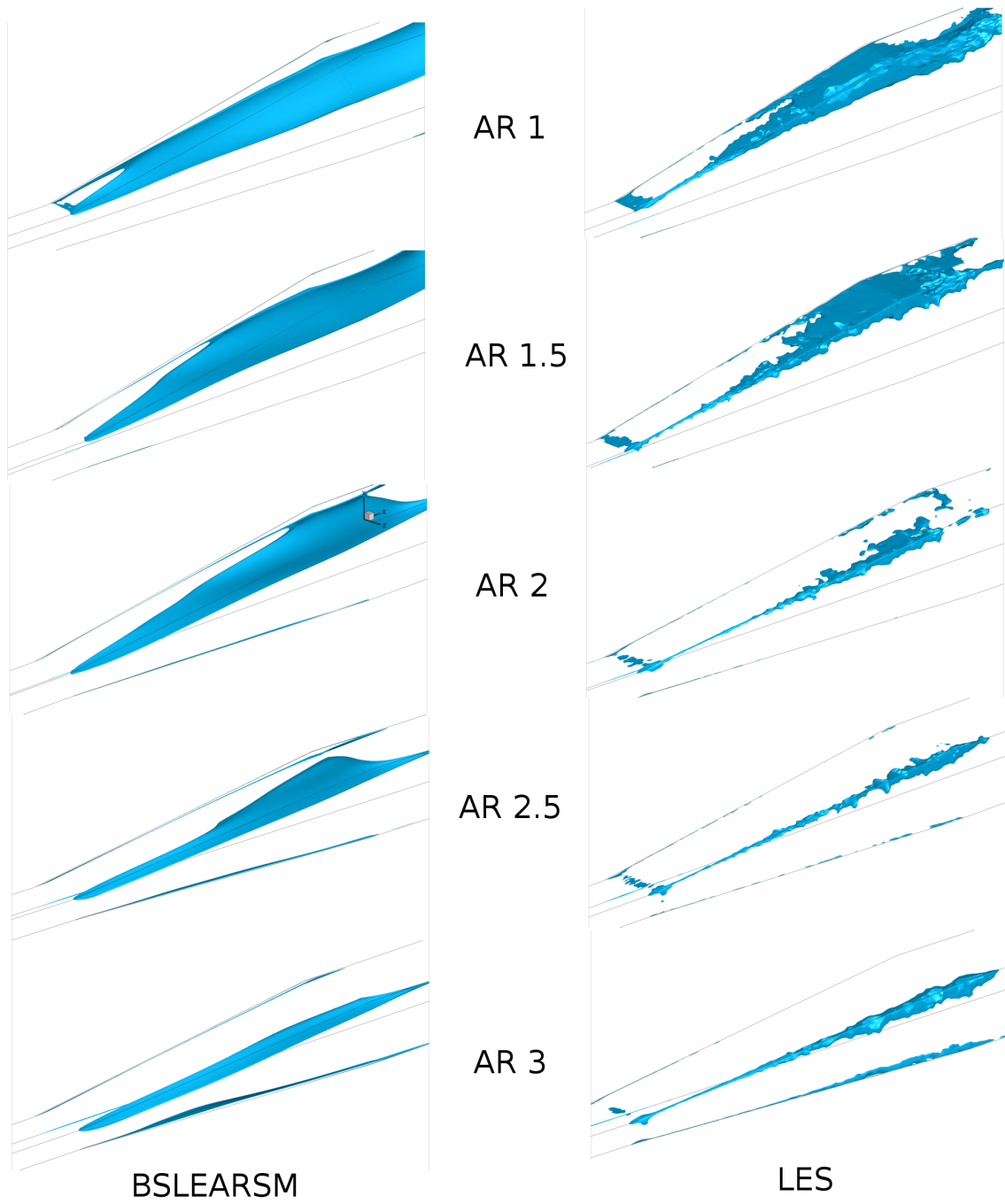
Figure 4.14   Separation topology in the family of diffusers predicted using an anisotropy-re-
solving BEARSM and LES
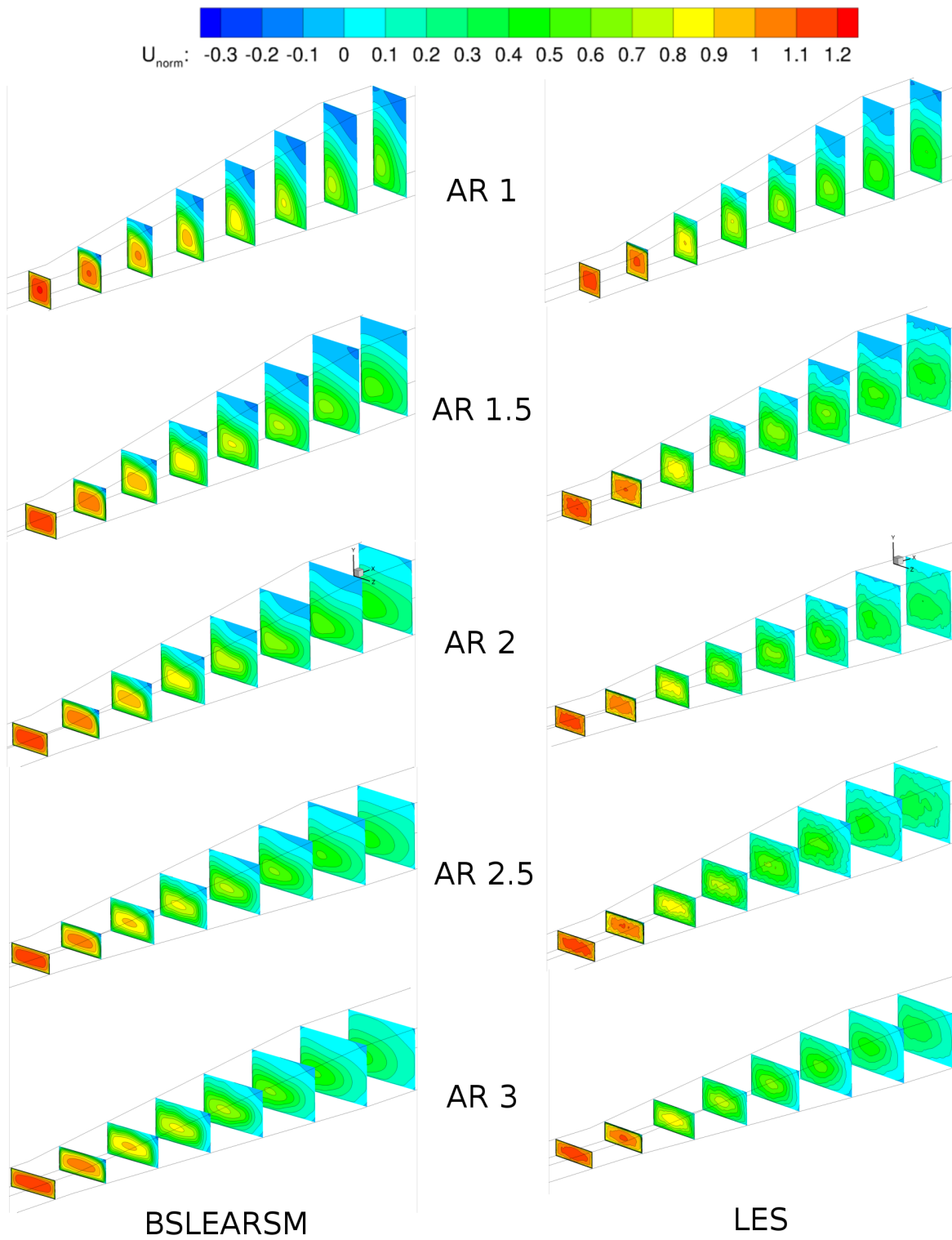
Figure 4.15 Streamwise mean velocity contours in the family of diffusers predicted by BEARSM and LES.

(a) BEARSM

(b) LES
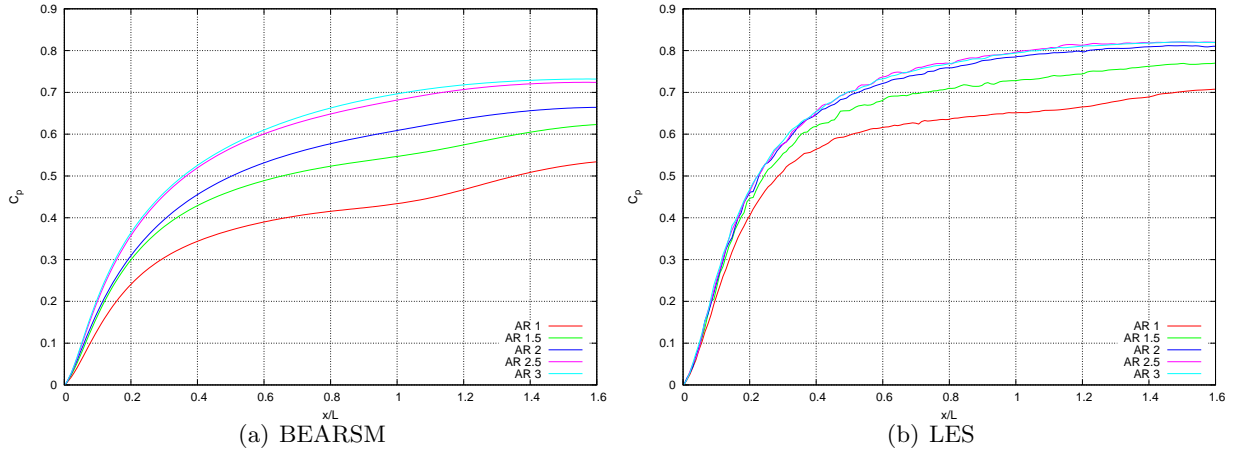
Figure 4.16   Pressure on bottom wall predicted by the BEARSM and LES. The abscissa is non-dimensionalized by diffuser length.

	A_1	A_2	A_3	A_4
EARSM-WJ2000(c_1=1.8, c_2=5/9)	1.2	0	1.8	2.25
Original LRR(c_1=1.5, c_2=0.4)	1.54	0.37	1.45	2.89
Linearized SSG	1.22	0.47	0.88	2.37

Table 4.1   ARSM coefficients for different linear Π_{ij}^r models

(a) original LRR

(b) linearized SSG
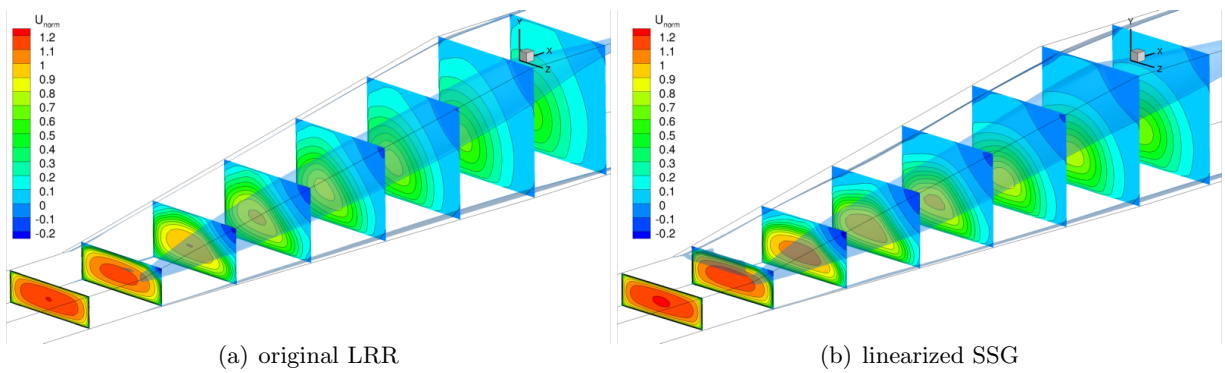
Figure 4.17   Separation predicted by two generalized linear EARSM.

is only generated by turbulence anisotropy. On comparison with DNS data of (Huser and Biringen, 1993), we notice the maximum turbulent kinetic energy to be under-predicted by 50%. Though the anisotropies are accurate, a weaker secondary flow is produced due to this inaccuracy as seen in Figure 4.18. The secondary streamlines show the direction to be accurate, however the V magnitudes are under-predicted.

(a) DNS V

(b) EARSM V

(c) DNS k

(d) EARSM k
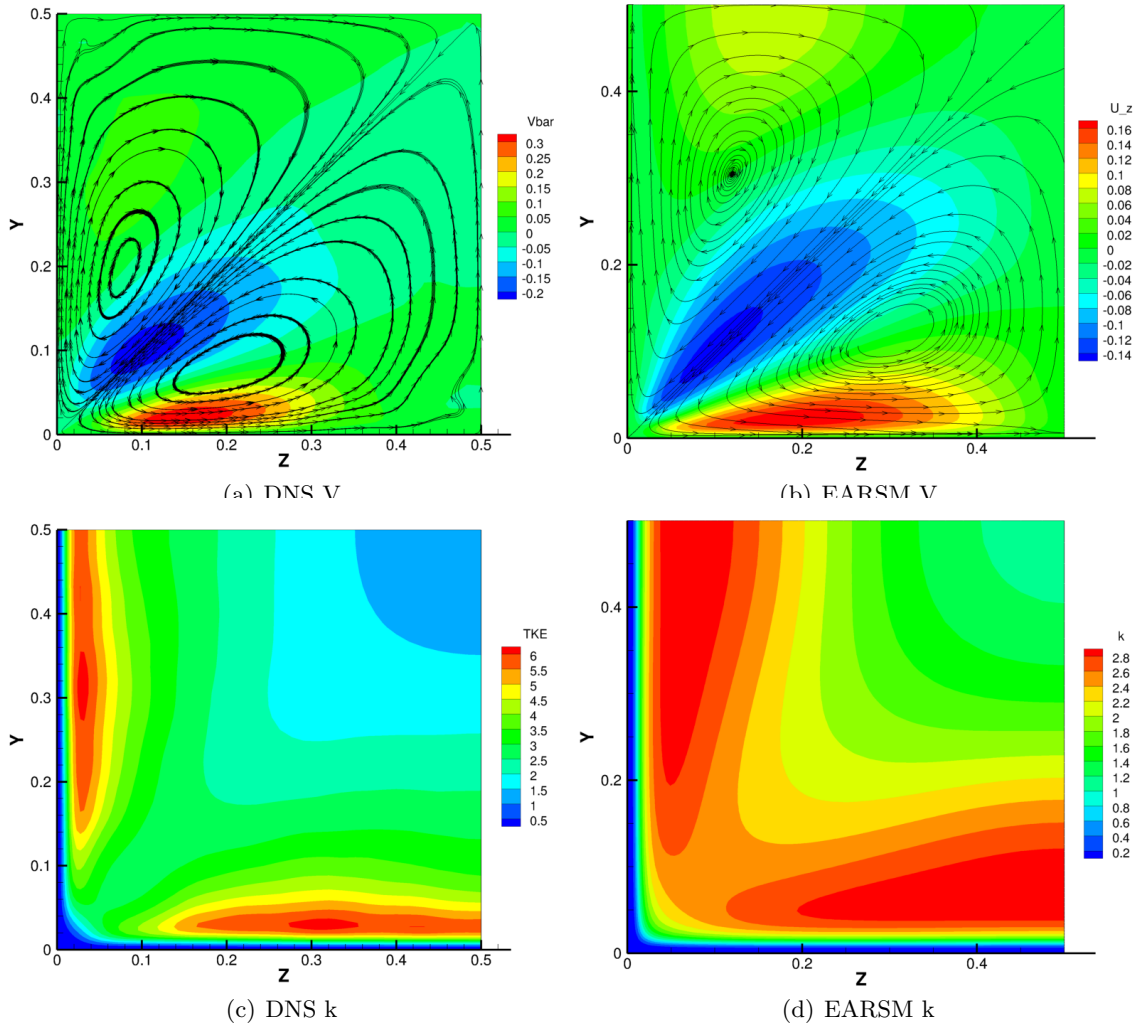
Figure 4.18   Secondary flow magnitude (V) and Turbulent kinetic energy (k) predicted by EARSM and compared with DNS data.

4.5.9 EARSM variants

Owing to the shortcomings of the BEARSM, a number of improvements to the model have been proposed. Each of them aimed at overcoming a particular simplification/assumption of the model, yet keeping the model computationally inexpensive and tractable. Few of these improvements have been implemented and tested for the baseline diffuser and their merits evaluated.

4.5.9.1 Diffusion correction

In regions of low $\mathcal{P}/\epsilon$ the convective and diffusion effects can be dominant. This is discussed in section 5 of Wallin and Johansson (2000). The modified coefficient on the LHS of the ARSM is modified to be;

$$c_1^{'} = \frac{9}{4}\left(C_1 - 1 - \frac{C_D}{\varepsilon}\frac{\partial}{\partial x}(\nu\frac{\partial}{\partial x}K)\right)$$

Approximating the turbulent diffusion to be balanced by production and dissipation, and approximating $\mathcal{P}/\epsilon = \beta_1 II_s$. The modification is only used in regions where production-dissipation ratio is less than one. Hence the constant is:

$$c_1^{'} = \frac{9}{4}\left(C_1 - 1 + C_D\mathrm{max}(1 + \beta_1^{eq}II_s, 0)\right)$$

Using this modified model, no major difference in the diffuser flow is noted(Fig.4.19. The modification applies only at about the core of flow due to the limiter. The secondary flow does capture the top left vortex which was seen in DNS, this top vortex was not resolved by BSL-EARSM and other models we used. The magnitude of the secondary flow is only 1% of U_{bulk} hence not a substancial improvement.

4.5.9.2 Calibration of Π_{ij} coefficients

The pressure-strain correlation $\Pi_{ij} = \overline{p(\partial_i u_j + \partial_j u_i)}$ is an important link is the accurate modeling of stresses. An exact solution for the rapid part is possible only for homogeneous flow, where equilibrium is considered. The coefficients for the widely used models Launder et al. (1975) and Speziale et al. (1991) are based on this fundamental flow. The objective of the calibration is to re-evaluate model coefficient for shear flows. The homogeneous parallel

(a) Mean flow velocity and separation surface

(b) Secondary flow at x/H=15
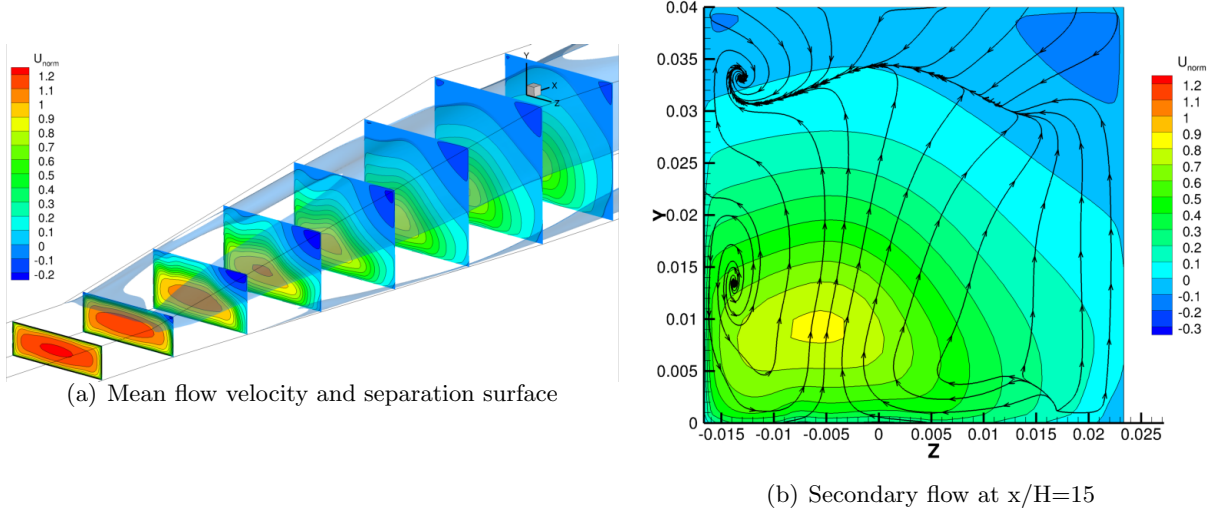
Figure 4.19   Flow predicted in the baseline diffuser using the diffusion-corrected EARSM

shear flow is considered, as the $\mathcal{P}/\varepsilon$ is known and an exact solution to the anisotropy transport equation exists (Durbin and Reif, 2000, Section 7.2). The existing models are used to predict the anisotropy and compare with experimently determined anisotropy for homogeneous shear given below;

$$\begin{pmatrix} 0.36 & -0.32 & 0 \\ -0.32 & -0.22 & 0 \\ 0 & 0 & -0.14 \end{pmatrix}$$

LRR(WJ used c=5/9,$c_1 = 1.8, c_2 = (c+8)/11 = 0.777, c_3 = (8c-2)/11 = 0.222$)

$$\begin{pmatrix} 0.296296 & -0.299977 & 0 \\ -0.299977 & -0.296296 & 0 \\ 0 & 0 & 0 \end{pmatrix}$$

For the calculations $\mathcal{P}/\varepsilon = 1.6$ was used as given by experiments. LRR WJ does not predict any a_{33} and the anisotropy of primary normal stress is under predicted. The SSG model assumes $c_1 = 1.7 + 0.9\mathcal{P}/\varepsilon$, with this the modified normal stress anisotropies are calculated. The a_{12} has an additional dependence on II_a, which is evaluated using the definition of second invariant. Choosing $\sqrt{II_a} = -0.438$ gives the principle shear stress anisotropy.

SSG(1991, $c_2 = 0.4125$ and $c_3 = 0.2125$)

$$\begin{pmatrix} 0.395722 & -0.257842 & 0 \\ -0.257842 & -0.28877 & 0 \\ 0 & 0 & -0.106952 \end{pmatrix}$$

Calibrating LRR model coefficients

As a_{12} is the most important anisotropy component for shear flows, this value can be fixed and rapid part coefficient 'c' can be found. This constraint gives c=0.505368, with this the anisotropy tensor is:

LRR(a_{12} matched, c_1=1.8)

$$\begin{pmatrix} 0.28413 & -0.32 & 0 \\ -0.32 & -0.26588 & 0 \\ 0 & 0 & -0.01825 \end{pmatrix}$$

A better comparison with experiments can be brought if a_{11} is also constrained. Notice that each of the components are dependent on only two coefficients for LRR, 'c' and 'c_1'. This additional constraint will fix c_1. As the coefficients are coupled, a simultaneous equation in these 2 coefficients is solved to arrive as their value **c=0.510289** and c_1=**1.30215** (A solution was eliminated using the constraint c > -2/3, which makes $b_{11} > 0$). The anisotropy tensor looks as:

LRR(a_{12} and a_{11} matched)

$$\begin{pmatrix} 0.36 & -0.32 & 0 \\ -0.32 & -0.339231 & 0 \\ 0 & 0 & -0.0207689 \end{pmatrix}$$

It is noticed that $a_{22} \gtrsim 16a_{33}$ which is 10 times the ratio found in experiments. This is inherent to the LRR modeling incompressibility assumption of $M_{ijkk} = 0$. It is interesting to note that c=5/9=0.5555 (WJ and Taulbee's assumption) is very close to the above predicted c.

With the new set of Corrected LRR coefficients(Table 4.2) the Generalized EARSM is solved for the baseline diffuser. The separation more accurately represents a total separation

	c_1	c_2	c_3
LRR (WJ2000)	1.8	0.77	0.22
Original LRR	1.8	0.763	0.109
Corrected LRR	1.302	0.7739	0.189
Linearized SSG	$1.7+0.9\frac{\mathcal{P}}{\varepsilon}$	0.4125	0.2125

Table 4.2 ARSM coefficients for the calibrated LRR and other linear Π_{ij} models

on the top wall as seen in Figure 4.20, than a corner separation as shown in Fig. 4.17. The accuracy of mean flow predicted is as good as the BEARSM approximation ($A_2 = 0$) with the inclusion of additional terms, however a more accurate C_p distribution is predicted with the Corrected coefficients(Figure 4.21). The correction has the following coefficients in Equation 4.11 $A_1 = 1.28$, $A_2 = 0.089$, $A_3 = 0.72$, $A_4 = 2.4$. Though A_2 is nearly zero, it has an influence on the accurate prediction of wall pressure. The observation challenges the assumption of c_2=5/9, adopted by Taulbee (1992) and Wallin and Johansson (2000).

(a) Mean flow velocity

(b) Secondary flow at x/H=15
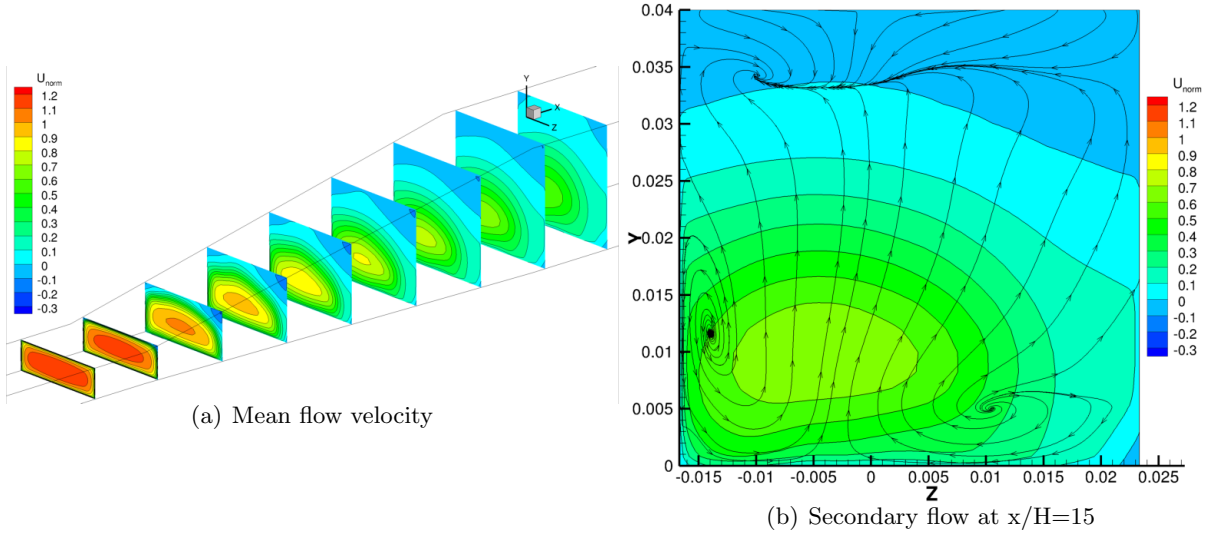
Figure 4.20 Flow predicted in the baseline diffuser using Generalized linear model with Corrected LRR coefficients
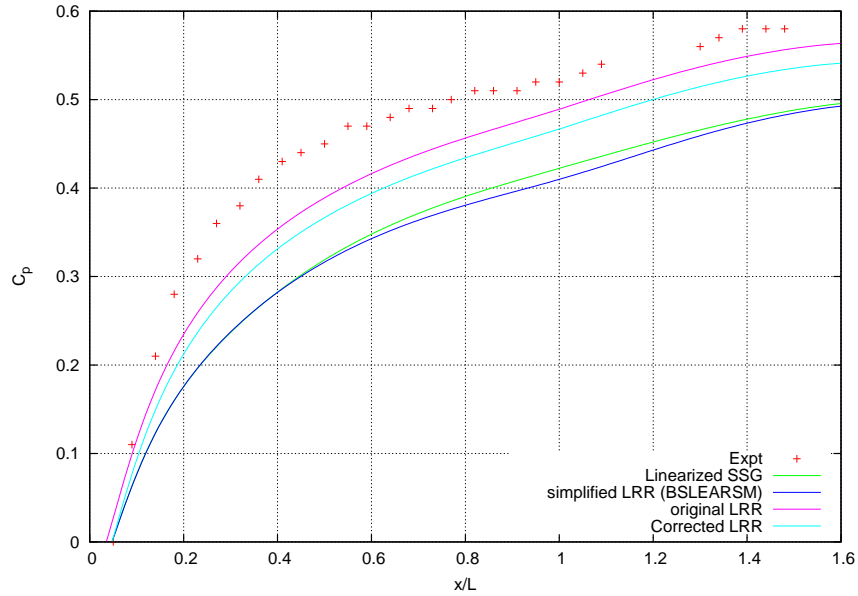
Figure 4.21　Wall C_p predicted by different Generalized EARSM models

4.5.9.3　Streamline curvature Correction

This correction is intended to predict the production accurately along a curved stream-line. This modifies the vorticity tensor $\mathbf{\Omega}$, with the rest of algebraic expressions the same as BEARSM. The Spalar-Shur(1997) model has been used to predict flow in the baseline flow, but to no improvement. The effects of streamline curvature on turbulence are negligible in the diffuser separation.

CHAPTER 5. CONCLUSION

The subject of 3-D flow separation is indeed challenging as it needs a fundamental understanding of various flow structures that interact to create the separated flow. The 3-D separated flow asymmetric diffusers is studied using the geometry of Cherry et al. (2008) as a reference. The experimental data has been used to validate the DES and the flow in the diffuser is studied using this eddy-resolving simulation. The linear eddy-viscosity RANS models fail to predict separation on the correct wall of 3-D diffuser. A set of diffusers parametrized by the inlet aspect ratio have been helpful in bringing out the flow and RANS model characteristics. The RANS models have been oversensitive to transverse pressure gradients, as separation switches from the one side wall to another with increasing aspect ratio, at lower aspect ratio than predicted by LES. Basically the RANS models predict the flow singularities correctly close to the diffuser inlet. However the secondary flow vortices dissipate faster downstream than is seen in SAS computations.

High resolution LES are conducted on the diffuser series to generate accurate mean and Reynolds stress predictions that can be used for model development. The LES of baseline diffuser predict accurately the flow as verified with the DNS dataset of Ohlsson et al. (2010). In order to predict the complex flow in diffusers, the effects of lateral straining, secondary flow of second kind needs to be resolved. Sensitizing the coefficient of eddy-viscosity (C_μ) was explored, however a more comprehensive model such as the Explicit algebraic RSM is found to predict separation accurately. The key of this RANS model is the ability to resolve the turbulence anisotropy from mean flow gradients. DNS data indicate the turbulence anisotropy to undergo an axisymmetric contraction in the separated region, while the rest of the flow undergoes axisymmetric expansion. An implementation of this model was used to predict the flow in baseline diffuser. Good agreement of mean flow quantities was observed with reference

to DNS data. The diffuser series showed the model to switch separation from top to side wall at nearly same $\mathcal{R}$ as observed in LES results, with the results more accurate than LEVM. As the model is developed from successive generalization of the RSM, the assumptions are clear and modeling improvements were done to improve prediction in diffusers. The EARSM predicts quantitatively the mean flow field accurately, however the Reynolds stresses are incorrect and wall pressure is under predicted. Recalibration of the pressure-strain tensor coefficients for original LRR was performed and an improved generalized EARSM model is developed which predicts a more accurate wall pressure coefficient. The effects of streamline curvature correction and diffusion correction were included in the model and tested for the diffuser flow, with no significant improvement in accuracy over the BEARSM of Menter et al. (2009).

5.1   Future work

Scope for improvement of the EARSM exists in enhanced modeling of the Pressure-strain rate term Π_{ij}, both slow and rapid part. Stress-strain relaxation effects need to be included to accommodate turbulence non-equilibrium. The model can also be adapted for the low range of SK/ε, such a modification would include non-local effects. Currently most models rely on a two-equation formulation for turbulence length scale, a novel approach is necessary to predict the near-wall behavior of the stresses in 3-D APG boundary layers. The LES dataset can be used to verify the Reynolds stress budgets and anisotropies predicted in the diffuser separation flow. There are a few existing improvement to EARSM that need to be tested for their efficacy in predicting 3D separated flows. A listing of the modeling enhancements that can be tested are given below:

Non-linear Pressure-strain modeling Till now most of the EARSM have used linear models or quasi-linear models, as the linearized SSG model. Non-linear models such as the Shih and Lumley (1985) and Fu et al (1987) can be used in the ARSM for Π_{ij}. An explicit solution to ARSM cannot be sought with a non-linear model. An effort was made by Gatski and Speziale (1993) to use a second-order model for Π_{ij}, however the quadratic term $\mathbf{a}^2$ had to be dropped to get an explicit form for $\mathbf{a}$. Regularization has

to be performed to avoid singularity in EARSM formulation. If a high-order $\mathbf{a}$ is used in the ARSM, the solution has to be numerically sought.

EARSM coefficients as functions of a The standard EARSM is given below with c_2 a constant. In the Wallin and Johansson (2000) model $c_2 = 5/9$ simplifying considerably the EARSM.

$$\left(c_1 - 1 + \frac{\mathcal{P}}{\varepsilon}\right)\mathbf{a} = -\frac{8}{15}\mathbf{S} + \frac{7c_2 + 1}{11}(\mathbf{a\Omega} - \mathbf{\Omega a}) - \frac{5 - 9c_2}{11}(\mathbf{aS} + \mathbf{Sa} - \frac{2}{3}\{\mathbf{aS}\}\mathbf{I}) \quad (5.1)$$

c_1 comes from the Rotta model and c_2 from the model used for pressure-strain correlation. The parameter c_2 has been suggested by Taulbee et al. (1994) to be dependent on invariants of $\mathbf{a}$ as

$$c_2 = \frac{2}{3}[1 - 2.2(1 + 0.8\sqrt{F})]$$

where $F = 1 + 27III_a + 9II_a$ and $II_a = -a_{kl}a_{lk}/8$ and $III_a = a_{kl}a_{lm}a_{mk}/24$. This formulation is recommended in the context of nonlinear model for pressure-strain, however it should be useful for linear models too.

Improved ARSM for low SK/ε An improvement to the standard ARSM was proposed by Taulbee (1992), which accounts for convection of strain $\frac{\mathcal{D}}{\mathcal{D}t}\left(\sqrt{II_S}\right)$. Improvements have been shown for non-equilibrium flows. A fourth term is added to the LHS coefficient of $\mathbf{a}$ in Equation 1.

$$\left(c_1 - 1 + \frac{\mathcal{P}}{\varepsilon} + \frac{\tau}{\sqrt{II_S}}\left[\frac{d(\sqrt{II_S})}{dt} + u_k\frac{d(\sqrt{II_S})}{dx_k}\right]\right)$$

where τ is the turbulence timescale and II_S is the second invariant of non-dimensional Strain. The EARSM can be solved using this modification.

Stress-strain lag model The model developed by Revell et al. (2006) accounts for lag by solving for an additional transport equation for $\frac{\mathcal{D}}{\mathcal{D}t}\left(\frac{\mathcal{P}}{\varepsilon}\right)$ and uses it to limit ν_T and calculate turbulence production $\widetilde{P_k}(= -k\frac{\mathcal{P}}{\varepsilon})$. The steps in this procedure are:

- calculate a_{ij} using the EARSM formulation
- Solve for C_{as}, which is $\frac{\mathcal{P}/\varepsilon}{\sqrt{2\mathbf{S}^2}}$. The boundary conditions for this term are 0 at wall. The author of model has used a wall damping function.
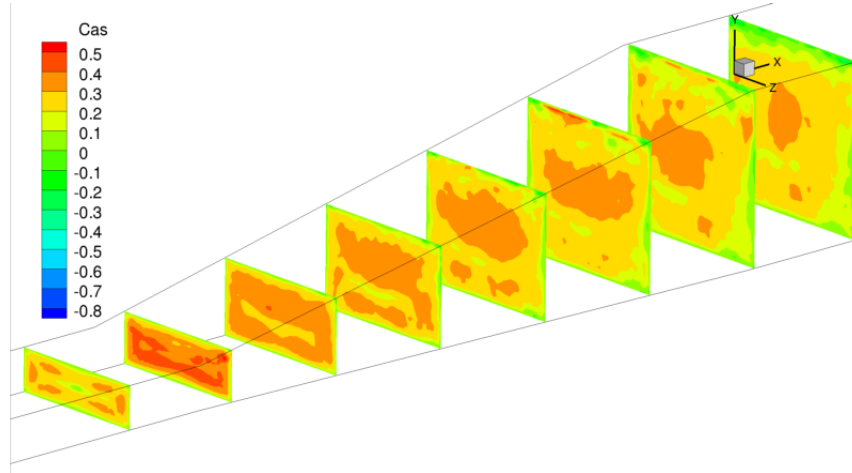
Figure 5.1 Stress-strain lag parameter $C_{as} = -\frac{a_{ij}S_{ij}}{\sqrt{2S_{ij}S_{ij}}}$ evaluated from LES flow field of baseline diffuser.

- solve for k and ω using updated production $\widetilde{P_k}$

- update ν_T=k min$\left(\frac{1}{\omega}, \frac{\mathcal{P}/\varepsilon}{4\mathbf{S}^2}\right)$

The lag parameter evaluated using LES (Fig. 5.1) indicates misalignment of stress and strain close to the diffuser inlet and at the walls.

BIBLIOGRAPHY

Abe, K.-I. and Ohtsuka, T. (2010). An Investigation of LES and Hybrid LES/RANS models for predicting 3-D diffuser flow. *Intl. J. of Heat and Fluid Flow*, pages 1–12.

Baba-Ahmadi, M. and Tabor, G. (2009). Inlet conditions for LES using mapping and feedback control. *Computers and Fluids*, 38(6):1299 – 1311.

Breuer, M., Aybay, O., Jaffrzic, B., Visonneau, M., Deng, G., Guilmineau, E., and Chikhaoui, O. (2009). Hybrid LESRANS-Coupling for Complex Flows with Separation. In Brun, C., Juv, D., Manhart, M., and Munz, C.-D., editors, *Numerical Simulation of Turbulent Flows and Noise Generation*, volume 104 of *Notes on Numerical Fluid Mechanics and Multidisciplinary Design*, pages 201–229. Springer Berlin / Heidelberg.

Buice, C. U. and Eaton, J. K. (2000). Experimental investigation of flow though an Asymmetric plane diffuser. *Journal of Fluids Enginnering*, 122:443–435.

Byun, G. and Simpson, R. L. (2006). Structure of Three-Dimensional Separated Flow on an Axisymmetric Bump. *AIAA Journal*, 44(5):999–1008.

Celik, I., Klein, M., and Janicka, J. (2009). Assessment Measures for Engineering LES Applications. *J. of Fluids Engineering*, 131:031102–1 to 031102–10.

Chapman, G. T. and Yates, L. A. (1991). Topology of flow separation on Three–dimensional bodies. *Applied Mechanics Review*, 44:329–345.

Cherry, E. M., Elkins, C. J., and Eaton, J. K. (2008). Geometric sensitivity of three–dimensional separated flows. *Intl. J. of Heat and Fluid Flow*, 29:803–811.

Cherry, E. M., Elkins, C. J., and Eaton, J. K. (2009). Pressure measurements in a three–dimensional separated diffuser. *International Journal of Heat and Fluid Flow*, 30:1–2.

Cherry, E. M., Iaccarino, G., Elkins, C. J., and Eaton, J. K. (2006). Separated flow in a three–dimensional diffuser: preliminary validation. Annual research briefs, Center for Turbulence Research, Stanford University.

Chong, Perry, and Cantwell (1990). A general classification of Three–dimensional flow fields. *Phys. Fluids*, 2:765–777.

Délery, J. M. (2001). ROBERT LEGENDRE AND HENRI WERLÉ: Toward the Elucidation of Three–Dimensional Separation. *Ann. Rev. Fluid Mechanics*, 33:129–154.

Durbin, P. A. (1996). On the $k - \epsilon$ stagnation point anomaly. *International Journal of Heat and Fluid Flow*, 17:89–90.

Durbin, P. A. and Reif, B. A. P. (2000). *Statistical Theory and Modeling for Turbulent flows*. John Wiley and Sons.

Gatski, T. and Speziale, C. G. (1993). On Explicit Algebraic Stress models for Complex Turbulent Flows. *Journal of Fluid Mechanics*, 254:59–78.

Gross, A. and Fasel, H. (2010). Hybrid RANS/LES Simulation of Turbulent Channel and Diffuser Flows. In *AIAA Sciences Meeting*.

Haimes, R. and Kenwright, D. (1999). On the Velocity Gradient Tensor and Fluid feature Extraction. In *AIAA 14th Computational Fluid Dynamics Conference*.

Huser, A. and Biringen, S. (1993). Direct Numerical Simulation of Turbulent flow in a Square Duct. *Journal of Fluid Mechanics*, 257:65–95.

Huser, A., Biringen, S., and Hatay, F. F. (1994). Direct simulation of turbulent flow in a Square duct: Reynolds-stress budgets. *Physics of Fluids*, 6(9):3144–3152.

Jeyapaul, E. and Durbin, P. (2010). Three–Dimensional Turbulent flow Separation in Diffusers. In *AIAA Sciences Meeting, AIAA 2010-918*.

Launder, B. E., Reece, G. J., and Rodi, W. (1975). Progress in the development of a Reynolds-Stress turbulence model. *Journal of Fluid Mechanics*, 68(3):537–566.

Menter, F. and Esch, T. (2001). Elements of Industrial Heat Transfer Predictions. In *16th Brazilian Congress of Mechanical Engineering (COBEM)*.

Menter, F. R. (1994). Two–equation Eddy–viscosity Turbulence models for Engineering Applications. *AIAA Journal*, 32:1598–1605.

Menter, F. R., Garbaruk, A. V., and Egorov, Y. (2009). Explicit Algebraic Reynolds Stress Models for Anisotropic Wall-Bounded Flows. In *EUCASS - 3rd European Conference for Aerospace Sciences, July 6-9th 2009, Versailles*.

Menter, F. R., Kuntz, M., and Bende, R. (2003). A Scale–Adaptive simulation for Turbulent flow predictions. *AIAA Paper 2003-0767*.

Nicoud, F. and Ducros, F. (1999). Subgrid-Scale Stress Modeling based on the Square of the Velocity gradient tensor. *Flow, Turbulence and Combustion*, 62:183–200.

Obi, S., Aoki, K., and Masuda, S. (1993). Experimental and Computational Study of Turbulent Separating flow in an Asymmetric plane Diffuser. In *Proceedings of the Ninth symposium on Turbulent Shear Flows*, page 305.

Ohlsson, J., Schlatter, P., Fischer, P. F., and Henningson, D. S. (2010). Direct Numerical Simulation of Separated flow in a Three–dimensional Diffuser. *Journal of Fluid Mechanics*, 650:1–12.

Pope, S. B. (1975). A more general effective–viscosity hypothesis. *Journal of Fluid Mechanics*, 72:331–340.

Revell, A. J., Benhamadouche, S., Craft, T., and Laurence, D. (2006). A Stress–Strain lag Eddy–viscosity model for unsteady mean flow. *International Journal of Heat and Fluid Flow*, 27:821–830.

Ryon, J. A. (2008). Computational simulation of Separated flow in a Three–dimensional diffuser using $\overline{v^2}$-f and ζ-f models. Master's thesis, Iowa State University.

Schneider, H., von Terzi, D., Bauer, H.-J., and Rodi, W. (2010). Reliable and Accurate prediction of Three–dimensional Separation in Asymmetric diffusers using Large Eddy simulation. *Journal of Fluids Engineering*, 132:031101–1 – 7.

Simpson, R. L. (1989). Turbulent Boundary–layer separation. *Ann. Rev. Fluid Mechanics*, 21:205–234.

Simpson, R. L. (1996). Aspects of Turbulent Boundary-layer Separation. *J. Fluids Engineering*, 32:457–521.

Speziale, C., Sarkar, S., and Gatski, T. (1991). Modelling the Pressure–strain correlation of Turbulence: an Invariant Dynamical systems approach. *Journal of Fluid Mechanics*, 227(-1):245–272.

Surana, A., Grundberg, O., and Haller, G. (2006). Exact theory of Three–dimensional flow separation. Part 1. Steady separation. *Journal of Fluid Mechanics*, 564:57–103.

Taulbee, D. B. (1992). An Improved Algebraic Reynolds Stress model and corresponding Nonlinear stress model. *Physics of Fluids*, 4(11):2555–2561.

Taulbee, D. B., Sonnenmeier, J. R., and Wall, K. M. (1994). Stress relation for Three–dimensional Turbulent flows. *Physics of Fluids*, 6:1399–1401.

Terzi, D., Schneider, H., and Frhlich, J. (2010). Diffusers with Three–Dimensional Separation as Test Bed for Hybrid LES/RANS Methods. In Nagel, W. E., Krner, D. B., and Resch, M. M., editors, *High Performance Computing in Science and Engineering '09*, pages 355–368. Springer Berlin Heidelberg.

Tobak, M. and Peake, D. J. (1982). Topology of Three–dimensional Separated flows. *Ann. Rev. Fluid Mechanics*, 14:61–85.

Törnblom, O. (2006). *Experimental and Computational studies of Turbulent Separating internal flows*. PhD thesis, KTH Mechanics.

Uribe, J., Revell, A., and Moulinec, C. (2010). Computation of Flow in a 3–D Diffuser Using a Two-Velocity Field Hybrid RANS/LES. In Deville, M., L, T.-H., and Sagaut, P., editors, *Turbulence and Interactions*, volume 110 of *Notes on Numerical Fluid Mechanics and Multidisciplinary Design*, pages 385–391. Springer Berlin / Heidelberg.

Van der Weide, E., Kalitzin, G., Schlüter, J., and Alonso, J. (2006). Unsteady Turbomachinery computations using massively parallel platforms. In *AIAA Paper 2006-421*.

Wallin, S. and Johansson, A. V. (2000). An Explicit Algebraic Reynolds stress model for Incompressible and Compressible Turbulent flows. *Journal of Fluid Mechanics*, 403:89–132.